GEOPHYSICS, VOL. 75, NO. 3 (MAY-JUNE 2010); P. MA9–MA26, 22 FIGS., 1 TABLE.
10.1190/1.3417757

Probabilistic microearthquake location for reservoir monitoring

Ran Xuan[1] and Paul Sava[1]

ABSTRACT

Accurately locating microseismic events can be used to monitor fluid migration during reservoir production and hydrofracturing operations. This is usually done with sparse networks of seismic sensors located in boreholes or with denser surface arrays. The data used for microearthquake monitoring are corrupted by noise, which reduces the signal-to-noise ratio to values as low as 0.1. Monitoring methods based on traveltime picking of various wave modes (P or S) cannot deal with this level of noise and require extensive user interaction. An alternative class of methods uses time reversal to focus microearthquake information at the source position. These methods can handle noisier signals because they do not rely on event picking or recorded seismograms, but the methods are also costlier to run and still require picking locations where wavefields focus. We advocate the time-reversal technique within the general framework of Bayesian inversion. Given an assumption about the possible locations of microearthquakes, we use recorded data to evaluate the feasibility of microearthquakes occurring at various locations in the earth. The method takes into account imaging imperfections caused by unknown components of the model or acquisition array aperture. We simulate wavefields corresponding to possible sources distributed in the model and evaluate their match with the wavefield reconstructed from the synthetic data recorded in the model. In this regard, the method operates like a pattern-recognition procedure and can exploit a wide variety of techniques designed for this purpose. We use simple crosscorrelation between simulated and reconstructed wavefields to take advantage of the speed and robustness of this technique. The wavefields reconstructed at various locations are used over time to scan the wavefield constructed from field data. Thus, our method can identify not only the position of the microearthquakes but also their origin times as well as the orientations of the fault planes characterizing the seismic sources. Maps of probability are the final outcome of this automated process, indicating the confidence of microearthquake occurrence at various positions and times.

INTRODUCTION

High-pressure fluid injected into oil and gas reservoirs causes time-invariant stress and strain changes. When elevated pore pressure reduces normal stress along faults, microseismic events are triggered by the release of shear stress along pre-existing fractures or through the creation of new fractures (Pearson, 1981; Maxwell and Urbancic, 2001; Duncan, 2005). Precise location of microseismic events is useful in monitoring hydraulic fracturing and for reservoir characterization (Rutledge and Phillips, 2003; Rentsch et al., 2004).

Most location methods currently used require the identification of seismic arrivals, which involves accurate picking of P- and S-wave arrival times. The origin time and the coordinates of the hypocenter of microseismic events are given by calculations that require accurate knowledge of the velocity model and of the physical relationships describing wave propagation in the subsurface. The source is located by optimizing a misfit function between measured and calculated quantities (Lay and Wallace, 1995; Thurber and Rabinowitz, 2000; Pujol, 2004). The methods in this category assume that the arrival time of a specific event can be identified on seismic traces (Gajewski et al., 2007). However, event identification is not always possible because of the low signal-to-noise ratio (S/N) characterizing microseismic events. Furthermore, such location methods strongly depend on the picking accuracy of P- and S-wave arrival times and have a low degree of automation (Rutledge and Phillips, 2003).

In contrast to the methods based on picked arrival times, migration-based methods use the full seismic wavefield to locate microseismic events. The main advantage provided by the methods in this category is that they are independent of the picking of specific arrivals and can locate weak events by focusing energy at the source using time reversal (Gajewski and Tessmer, 2005). The drawback of methods in this category is the high computational cost that limits their practical use. However, this drawback becomes less and less

Manuscript received by the Editor 18 May 2009; revised manuscript received 4 December 2009; published online 3 June 2010.
[1]Colorado School of Mines, Center for Wave Phenomena, Golden, Colorado, U.S.A. E-mail: rxuan@mines.edu; psava@mines.edu.
© 2010 Society of Exploration Geophysicists. All rights reserved.

Downloaded 16 Jul 2010 to 138.67.12.184. Redistribution subject to SEG license or copyright; see Terms of Use at http://segdl.org/

significant because of advances in computer hardware, which allow for fast processing of large volumes of data.

Within the context of migration-based methods, we advocate a new methodology that can be used to automatically identify and locate sources of microseismicity. We use time reversal based on numeric solutions to the elastic wave equation to reconstruct seismic wavefields in the space around the possible source position and around the possible origin time of seismic events. Ideally, the energy corresponding to a microseismic event focuses at some time and some position in space. However, because of the incomplete acquisition, inaccuracies of the velocity model, and noise present in data, this focus is hard to identify or may not even form at all.

We address this problem by constructing at various locations in the model and at various times "ideal" wavefields which we would record given the field-acquisition geometry and the velocity model in the region under investigation if a microearthquake source would be located at that position, time, and fault orientation. We address this problem by constructing ideal wavefields at various locations in the velocity model. We use these wavefields to evaluate whether a microearthquake source would be located at that position, and at various times. We also use these wavefields to determine the fault orientation given the field-acquisition geometry and the velocity model in the region under investigation. Then we employ a pattern-matching procedure to compare the reconstructed wavefields based on field data with our simulated wavefields and identify the most probable locations and origin times of microseismic events. This process exploits the kinematic properties of the focused wavefields and takes advantage of the distortions caused by incomplete acquisition in the area under investigation.

Given the uncertainty characterizing the process of microearthquake identification, we do not construct our results as precise positions, origin times, and fault-plane orientation. Instead, we construct maps of probability indicating the likelihood that a microseismic source exists at a given position, at a given time, and with a given orientation. We construct our solutions using Bayesian inversion theory, which simply states that inversion is a process that refines our state of knowledge.

AUTOMATIC MICROEARTHQUAKE IDENTIFICATION

A procedure for microearthquake monitoring addresses the following questions: What is the position in space where the microearthquake occurred? At what moment in time did the microearthquake occur? What type of source characterizes the observed microearthquake? Ideally, these questions should be addressed using an automatic procedure based on the data recorded in the vicinity of the zone in which microearthquakes are most likely to occur.

Designing such an automatic procedure is difficult because of several factors. First, the monitoring array usually covers a small region in space (perhaps a short interval in a borehole) and may be relatively sparse with respect to the observed wavefields. Therefore, the angular coverage that controls the accuracy and resolution of the spatial location is small, leading to partially focused energy at the source. Second, the model used for propagation toward the source is typically not known with sufficient accuracy. Therefore, even assuming that we acquire data with a wide enough array, it is possible that the recorded energy does not focus completely at the true source position. Third, the recorded data are typically noisy, sometimes characterized by a signal-to-noise ratio smaller than 1. In this case, the microearthquake events cannot be identified (i.e., picked) on recorded data using ray-based methods. A better strategy is to backpropagate all recorded data toward the source and allow the low-energy signal to focus at the source. In the time-reversal process, the noise does not accumulate constructively, thus improving the signal-to-noise ratio and making event identification possible. However, the signal may still be partially obstructed by the noise, even after wave-equation back propagation toward the source.

Because of all the sources of uncertainty mentioned earlier, the microearthquake focus we obtain by back propagation toward the source does not have the expected characteristics of an ideal experiment. Furthermore, the partial focus for a given event depends on position in space, i.e., the relative position of the microearthquake to the recording array. An automatic procedure needs to address this reality and seek to resolve, at least partially, the uncertainty and ambiguity characterizing the microearthquake source identification.

Our proposed solution is to reformulate the question underlying the source-identification process. Instead of seeking to find the position and trigger time for a given event, we seek to construct time-varying maps of probability which indicate the likelihood that a microearthquake occurred at a location in space, given the limited data available, the model uncertainty, and the noise present in the data. Following the construction of the probability maps, we could identify the most likely location, along with a region of confidence.

We address this problem by using Bayesian inversion theory, which uses probability density functions (PDFs) as a measurement of a given state of knowledge (Jaynes, 2003). A crucial feature of Bayesian theory is that a probability can be assigned to a hypothesis. For example, we can assume that microearthquakes occur in a given region in space with certain probability provided by all our knowledge about the surrounding geology and the processes leading to the microearthquake. According to the Bayesian theory, we begin our investigation with a certain state of knowledge that is independent of any subsequent measurement we make. We assign to any possible model that is acceptable based on our prior state of knowledge a likelihood that quantifies how probable that particular model is to correspond to reality (Tarantola, 2005).

For example, we could use a priori information to decide what is the most likely region and period in which microearthquakes occur due to geologic constraints (e.g., fracture zones) or borehole activities (e.g., interval and time of fracturing). The posterior state of information combines our prior understanding of the model parameters with additional information derived from measurements and assumptions about the physical laws governing the process under investigation. This approach allows us to incorporate any a priori information in the data, parameters, and theory. For example, we could use recorded data to refine the region and period in which microearthquakes occur. The posterior model can become the prior model for another experiment, and thus, more data can recursively refine the model and lead to a better definition of the interval in which microearthquakes are triggered.

As discussed by Tarantola (2005), the posterior state of information is obtained using Bayes' theorem

$$\sigma(\mathbf{m},\mathbf{d}) = k\frac{\rho(\mathbf{m},\mathbf{d})\,\Theta(\mathbf{m},\mathbf{d})}{\mu(\mathbf{m},\mathbf{d})}, \tag{1}$$

where $\mathbf{m}$ and $\mathbf{d}$ represent the model and the data, $\rho(\mathbf{m},\mathbf{d})$ is the a priori state of information, $\Theta(\mathbf{m},\mathbf{d})$ is the theoretical state of information, $\mu(\mathbf{m},\mathbf{d})$ is the homogeneous state of information, k represents a

Downloaded 16 Jul 2010 to 138.67.12.184. Redistribution subject to SEG license or copyright; see Terms of Use at http://segdl.org/

normalization constant, and $\sigma(\mathbf{m},\mathbf{d})$ is the a posteriori state of information. According to equation 1, the a posteriori state of information $\sigma(\mathbf{m},\mathbf{d})$ is computed by combining the theoretical function $\Theta(\mathbf{m},\mathbf{d})$ with the prior information $\rho(\mathbf{m},\mathbf{d})$. The solution to the inversion problem is given by $\sigma_{\mathfrak{M}}(\mathbf{m})$, which represents the posterior marginal probability on the model space and is obtained by integrating the a posteriori probability density function over data:

$$\sigma_{\mathfrak{M}}(\mathbf{m}) = \int_{\mathfrak{D}} \sigma(\mathbf{m},\mathbf{d}) d\mathbf{d} \tag{2}$$

where $\mathfrak{D}$ is the data space. A summary of Bayesian inversion theory is presented in Appendix A.

As emphasized by equation 1, a key component of applying Bayesian inversion for the microearthquake location problem is the conjunction of the prior and theoretical probability density functions to obtain the posterior probability density function, which in practical terms reduces to finding the set of model parameters which corresponds to the same data (Figure A-1 and Figure A-2 in Appendix A). As we discuss in detail in the following sections, this idea can be implemented for microearthquake monitoring by finding the similarity between wavefields simulated from various locations in the image space (the idealized theoretical PDF) and comparing them to wavefields reconstructed from recorded data (the idealized prior PDF). This procedure can be implemented using different image-processing procedures, one possibility being normalized crosscorrelation. We compute the crosscorrelation between the theoretical and reconstructed wavefields at various locations in the model as well as at various moments in time. When the crosscorrelation maximizes, we conclude that we have identified a likely location and time of a microearthquake. This automatic procedure naturally takes into consideration the limited event aperture as well as the approximate knowledge of the model used for wave propagation.

The microearthquake identification problem is further complicated by the fact that we do not know the exact mechanism of the source. This is an unavoidable complication because the source mechanism changes the type of focus we are looking for in our automatic identification process. Identifying the source mechanism is important because it gives us insight into the physical processes leading to the microearthquake. Given the limited receiver aperture and the uncertainty in the model used for back propagation, the reconstructed wavefields generally cannot provide us with information about the exact radiation pattern of the source. What we can hope for is to find the most likely source mechanism by matching wavefields distorted by the acquisition array, similar to the procedure by which we identify the most likely position and trigger time of the source. The requirement is that we incorporate the source mechanism in the theoretical wavefields used in the crosscorrelation.

We discuss this procedure in full detail in the following sections and provide 2D and 3D examples for elastic and acoustic data.

BAYESIAN MICROEARTHQUAKE MONITORING

According to Bayesian inversion theory, the locations corresponding to microseismic events are provided by incorporating information from recorded seismograms with prior information on the events, e.g., possible locations and origin time of the events as well as physical relations between the model and data.

We simulate microearthquakes using the double-couple source mechanism characterizing slip fractures (Figure 1). The model parameters used for the microearthquake location problem are $\mathbf{m} = \{\mathbf{x},\tau,\theta\}$, where $\mathbf{x} = \{x,y,z\}$ describes the position of a microseismic event in space, τ describes the origin time, and θ describes the orientation of the fracture characterized by the double-couple source relative to the horizontal axis. In three dimensions, we would have to use two angles to characterize the fault-plane orientation. The data $\mathbf{d}$ represent the wavefields reconstructed from recorded seismograms in the space around the most probable microearthquake source locations and origin times. In this context, it is irrelevant whether the data are acquired in a borehole, on the surface, or by using a combination of borehole and surface arrays. The data parameters $\mathbf{d}(\mathbf{x},t)$ are subsets of the reconstructed wavefields. Each model has only one datum because there is one wavefield characterizing one microseismic event in space and time for a given fault-plane orientation. The kernel function $G(\mathbf{m})$ describes the theoretical relationship between the data and the model. As discussed earlier, we evaluate data for all possible models by taking into consideration the velocity in the region under investigation and the acquisition geometry used for the field experiment. In our case, the kernel function is based on the two-way elastic wave equation and is constructed using the following steps:

(1) For a given model ($\mathbf{m}$) characterized by the origin time τ, source location $\mathbf{x}$, and fault plane orientation θ, we propagate waves forward from the source using the velocities $V_{P0}(\mathbf{x})$ and $V_{S0}(\mathbf{x})$ according to the two-way elastic wave equation

$$\rho\ddot{\mathbf{u}} - (\lambda_0 + 2\mu_0)\nabla(\nabla\cdot\mathbf{u}) + \mu_0\nabla\times\nabla\times\mathbf{u} = \mathbf{f}(\mathbf{m},t), \tag{3}$$

where $f(\mathbf{m},t)$ is the considered source wavelet, $\mathbf{u}(\mathbf{x},t)$ is the seismic wavefield simulated forward in time, $\lambda_0 = \rho(V_{P0}^2 - 2V_{S0}^2)$, and $\mu_0 = \rho V_{S0}^2$, where ρ is the medium density which we assume to be constant, for simplicity.

(2) The forward wavefield is recorded at receiver coordinates $\mathbf{x}_0$, arbitrarily located in space:

$$\mathbf{r}(\mathbf{x}_0,t) = \mathbf{u}(\mathbf{x} = \mathbf{x}_0,t), \tag{4}$$

where $\mathbf{r}(\mathbf{x}_0,t)$ represents the recorded seismogram.

(3) The recorded seismogram is time-reversed and back-propagated in time from the acquisition array to reconstruct the wavefield at all locations in space and all times within the window considered for our prior model. This step is also based on the two-way elastic wave equation 3, where the source function is replaced by the time-reversed recorded data at the receiver coordinates.

Then we store the back-propagated wavefields in the immediate vicinity of the source and around the known origin time. For a given model, we refer to the wavefields calculated using this procedure as the predicted data $\mathbf{d}^{\text{pre}}$. In contrast, we refer to the wavefields reconstructed from field seismograms as the observed data $\mathbf{d}^{\text{obs}}$. The predicted data $\mathbf{d}^{\text{pre}}$ and observed data $\mathbf{d}^{\text{obs}}$ are similar to one another only

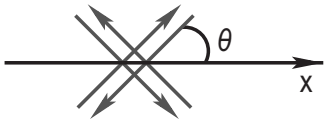


Figure 1. Schematic representation of a double-couple source with an orientation of θ relative to the horizontal direction.

Downloaded 16 Jul 2010 to 138.67.12.184. Redistribution subject to SEG license or copyright; see Terms of Use at http://segdl.org/

at the location of the source, at the origin time, and at the correct orientation of the fault plane. In this way, we can use the predicted wavefields as a template to which we compare the observed wavefields to identify the position, time, and fault orientation of the microseismic source.

We illustrate our method with a 2D synthetic example. We assume that we use the P-wave velocity shown in Figure 2a and S-wave velocity shown in Figure 3a as the background velocity to construct the predicted data using the procedure outlined in the preceding paragraphs. We consider the velocity shown in Figures 2b and 3b as the true velocities, which are used to simulate the field seismograms. We simulate data by considering a double-couple microseismic source at $\mathbf{m}_t = \{x_t, z_t, \tau_t, \theta_t\}$, where the subscript t indicates the true position of the source. The acquisition array consists of 19 receivers on the surface. We simulate a seismic source at $x = 0.136$ km and $z = 0.334$ km.

The wavefield simulated for one event is calculated using the elastic wave equation 3 using $\lambda = \rho(2V_P^2 - V_S^2)$ and $\mu = \rho V_S^2$. Here, $V_P(\mathbf{x})$ and $V_S(\mathbf{x})$ are the real medium parameters, which are different from the background medium parameters, $V_{P0}(\mathbf{x})$ and $V_{S0}(\mathbf{x})$, used for simulation of the expected wavefields. The real medium parameters are assumed to be unknown during the inversion process. The simulated synthetic seismogram is shown in Figure 4, in which 4a and 4b depict the vertical and horizontal components, respectively. The data are corrupted by noise with an S/N approximately equal to 3.

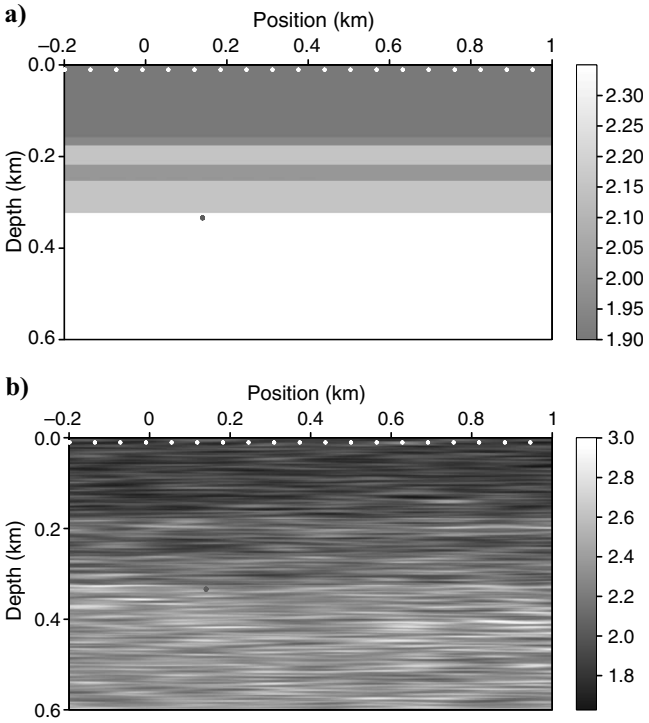


Figure 2. P-wave velocities used (a) to compute the kernel function and (b) to simulate data. The random velocity in panel (b) is the sum of the velocity in model (a) with correlated Gaussian noise with a magnitude of 40% of the background. The background velocity model is sampled every 1 m and ranges between 1.9 and 2.4 km/s. The dots located at the top of surface and at the middle of the velocity model represent the locations of receivers and source, respectively.

The prior information on the model

We assume that the hypocenter and the origin time of microseismic events may be located with equal probability within a certain

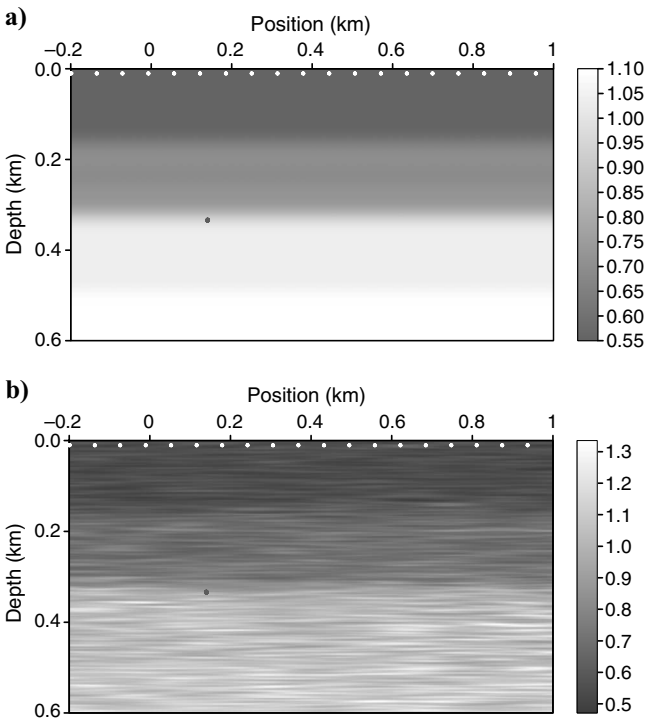


Figure 3. (a) Velocity model used for the kernel function and (b) velocity model with random variability used to simulate data. The random velocity in panel (b) is the sum of the velocity in model (a) with correlated Gaussian noise with a magnitude of 40% of the background. The background velocity model is sampled every 1 m and ranges between 0.5 and 1.1 km/s. The dots located at the top of surface and at the middle of the velocity model represent the locations of receivers and source, respectively.

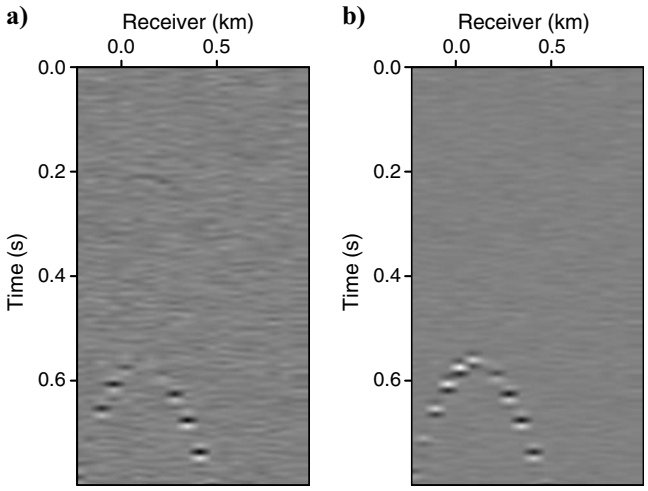


Figure 4. Synthetic seismogram simulated using the velocity model shown in Figures 2b and 3b. Parts (a) and (b) depict the vertical and horizontal components of the recorded wavefield, respectively. We consider an absorbing boundary condition at the top of the model. The double-couple source used to simulate this event is a Ricker wavelet with a dominant frequency of 30 Hz. A total of 8000 time steps with a time increment of 0.1 ms is calculated.

Downloaded 16 Jul 2010 to 138.67.12.184. Redistribution subject to SEG license or copyright; see Terms of Use at http://segdl.org/

space domain, a certain time interval, and at all possible fault-plane angles. Thus, we describe this prior knowledge on the model space as a boxcar function in space, time, and fault-plane angle. The prior probability $\rho_{\mathfrak{M}}(\mathbf{m})$ equals one within this region of space and time and equals zero elsewhere. We uniformly sample the model space within this region. The number of models located in this space is $n_x \times n_z \times n_\theta$, where n_x and n_z represent the model indexes along the x- and z-axes, respectively, and n_θ represents the number of sampled plane orientations. In our example, we sample the model parameters every 4 m and at every fifth degree. Some of the locations for which we simulate data using our procedure are shown in Figure 5. By selecting a finite number of possible source positions, we exploit our knowledge about the true source location and reduce computational time. The assumption we make here is that the data (reconstructed wavefield corresponding to the recorded seismograms) characterize with equal probability for all models within our selected model space, as illustrated in Figure A-1a in Appendix A. More generally, we could consider that models are more probably distributed along geologic features, thus exploiting prior information in inversion.

The theoretical information on model and data

For all models within our selected region of space, we compute the corresponding wavefield by the forward/backward procedure outlined in the preceding section. In our case, we assume that each model corresponds to one data set and that all simulated wavefields are equally probable to explain the observed wavefields. This construction, which corresponds to the illustration in Figure A-1b in Appendix A, applies the kernel functions G that theoretically link individual members of the model and data spaces. We assemble all those calculations in a database of wavefields that is used to compare data reconstructed from the field seismograms.

We consider several possible strategies for imaging with recorded elastic data. One possibility is to reconstruct the wavefield in the entire imaged volume using the elastic wave equation and the full elastic wavefield. In this case, we can construct wavefield databases at various locations in space that correspond to the vertical and horizontal components of the wavefield. Alternatively, we can consider just the vertical component of the recorded seismograms and use it to reconstruct the acoustic wavefields in the entire imaged volume using the acoustic wave equation. In this case, we reconstruct wavefield databases corresponding to different wave velocities (e.g., P- or S-wave modes) at various locations in space.

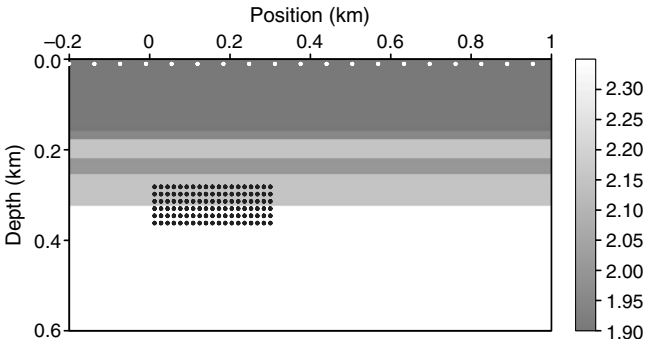


Figure 5. Schematic representation of the a priori information on the model space. We assume that microearthquakes occur in the region indicated by the dense dots between $x = 0-0.35$ km and $z = 0.25-0.35$ km. A similar discrete set of possible origin times is defined along the time axis.

Figures 6 and 7 illustrate the wavefield databases at one location indicated by dots in Figure 5. Figure 6a and 6b corresponds to the vertical and horizontal components of the wavefield reconstructed using the elastic wave equation, respectively. Figure 7a and 7b corresponds to the acoustic wavefields reconstructed using the acoustic wave equation from the vertical component of the recorded seismo-

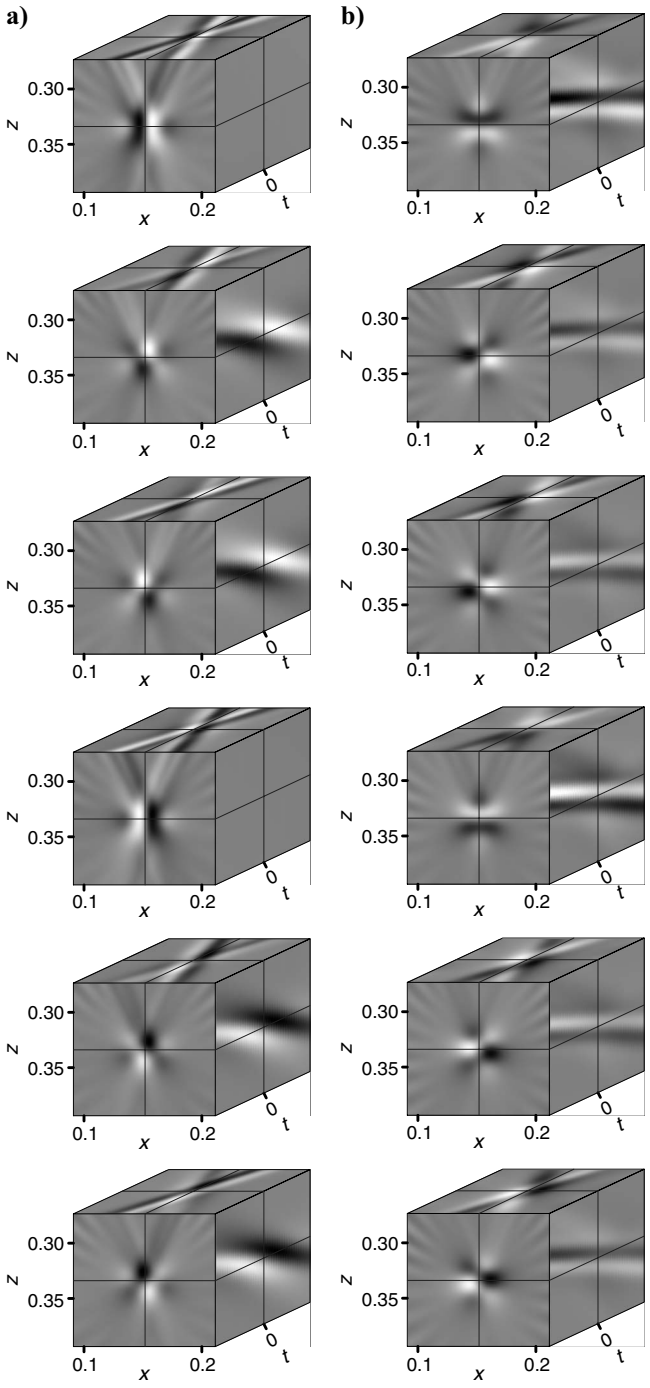


Figure 6. Seismic wavefield database for the (a) vertical and (b) horizontal components of the wavefield reconstructed using the elastic wave equation. All panels correspond to a specific position in space for various orientations of the double-couple source plane. A similar database can be constructed for other locations.

Downloaded 16 Jul 2010 to 138.67.12.184. Redistribution subject to SEG license or copyright; see Terms of Use at http://segdl.org/

gram using the P-wave and S-wave velocities, respectively. The size of the cubes in Figures 6 and 7 is two wavelengths in space and two periods in time.

The kernel functions constructed with this procedure are functions of the velocity, the acquisition geometry, and the source type. We refer to the predicted data calculated from the models defined by $\rho_{\mathcal{M}}(\mathbf{m})$ for the fixed velocity model, layout of receivers, and source type as the reconstructed wavefield database. This database needs to be calculated only once if we keep the subsurface velocity and acquisition geometry fixed.

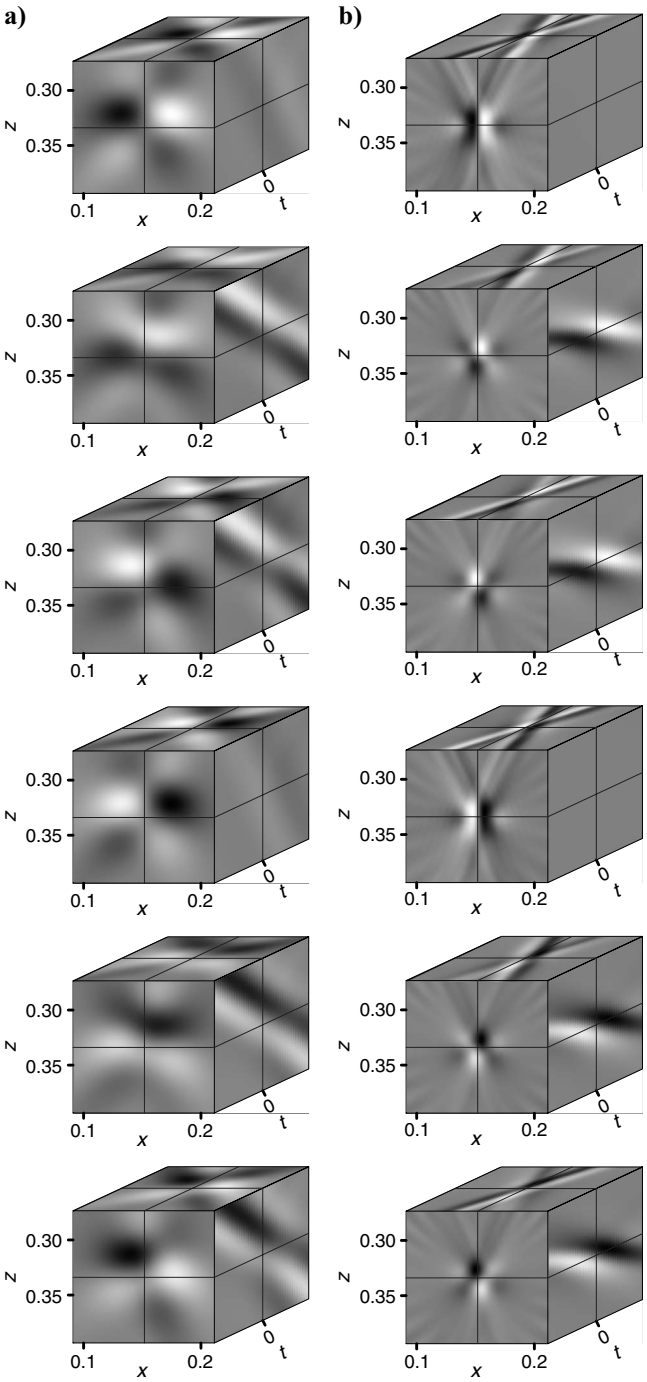


Figure 7. Seismic wavefield database corresponding to wavefield reconstruction using the acoustic wave equation based on the vertical component of the recorded data as a source and the (a) P-wave and (b) S-wave velocities for propagation. All panels correspond to a specific position in space for various orientations of the double-couple source plane. A similar database can be constructed for other locations.

If two sources are located at the same position but have different origin times, the refocused fields of these two events are the same. It is sufficient to compute wavefields for one origin time and then compare these simulated wavefields with the wavefields reconstructed from field seismographs at various times. Thus, we not only can identify the location of the source but we also can identify the origin time. Furthermore, we could identify the source type by comparing the reconstructed wavefields with the database computed for different sources.

In an ideal case, if the sources are explosive and are completely surrounded by receivers, the wavefronts reconstructed by time reversal should focus into a point at the source location and origin time. However, in this paper, we consider double-couple sources. The focus of the reconstructed wavefield is not a point; it follows the radiation pattern of the source and depends on the orientation of the fault plane. The fault orientations in Figures 6 and 7 are, from top to bottom, 0°, 30°, 60°, 90°, 120°, and 150°, respectively. The size of the focus shown in Figure 7a is larger than that of the focus shown in Figure 7b because the P-wave wavelength is larger than the S-wave wavelength, assuming equal frequency content of the signal describing the two wave modes. The focus shown in Figure 6a is similar to that shown in Figure 7b because the elastic wavefield is dominated by the S-wave mode.

The prior information on the data

As discussed previously, we refer to data as reconstructed wavefields at all locations in space and within a given time window. We loop over the models provided by $\rho_{\mathcal{M}}(\mathbf{m})$ and look for the times and locations in space where data reconstructed from recorded seismograms match the simulated data at locations where we assume that microseismic events are located. We can conceptually describe the process as measuring the similarity between multidimensional images. Various methods can be used to compare the similarity between the predicted data and the observed data. These methods include crosscorrelation, sum-of-squared differences, and ratio image uniformity, which are three of the most common area-based methods used in medical-image registration to compare the images of the same modality (Zitová and Flusser, 2003).

In this work, we use normalized crosscorrelation (N_{cc}) to measure the similarity between theoretical wavefields and wavefields reconstructed from field seismograms. By definition, we compute normalized crosscorrelation for vector wavefields by the expression

$$N_{cc}(\mathbf{m}) = \frac{\sum_{\mathbf{x}-M_{\mathbf{x}}}^{\mathbf{x}+M_{\mathbf{x}}} \sum_{t-M_t}^{t+M_t} (\mathbf{d}^{obs} - \overline{\mathbf{d}^{obs}}) \cdot (\mathbf{d}^{pre} - \overline{\mathbf{d}^{pre}})}{\sqrt{\sum_{\mathbf{x}-M_{\mathbf{x}}}^{\mathbf{x}+M_{\mathbf{x}}} \sum_{t-M_t}^{t+M_t} \|\mathbf{d}^{obs} - \overline{\mathbf{d}^{obs}}\|^2} \sqrt{\sum_{\mathbf{x}-M_{\mathbf{x}}}^{\mathbf{x}+M_{\mathbf{x}}} \sum_{t-M_t}^{t+M_t} \|\mathbf{d}^{pre} - \overline{\mathbf{d}^{pre}}\|^2}} \quad (5)$$

and for scalar wavefields (or perhaps one component of the vector wavefields) by the expression

Downloaded 16 Jul 2010 to 138.67.12.184. Redistribution subject to SEG license or copyright; see Terms of Use at http://segdl.org/

$$N_{cc}(\mathbf{m}) = \frac{\sum_{\mathbf{x}-M_x t-M_t}^{\mathbf{x}+M_x t+M_t} \sum (d^{obs} - \overline{d^{obs}})(d^{pre} - \overline{d^{pre}})}{\sqrt{\sum_{\mathbf{x}-M_x t-M_t}^{\mathbf{x}+M_x t+M_t} \sum (d^{obs} - \overline{d^{obs}})^2} \sqrt{\sum_{\mathbf{x}-M_x t-M_t}^{\mathbf{x}+M_x t+M_t} \sum (d^{pre} - \overline{d^{pre}})^2}}, \quad (6)$$

where the overline denotes average values, $\mathbf{d}^{obs}$ or d^{obs} are the observed data, and $\mathbf{d}^{pre}$ or d^{pre} are the predicted data. The size of the averaging window is $(2M_x + 1) \times (2M_t + 1)$, where $\mathbf{x} = \{x,y,z\}$. The normalized crosscorrelation is evaluated at the locations of every model $\mathbf{m}$. The values of N_{cc} are between -1 and $+1$. Using this equation, we pinpoint the model that generates the highest N_{cc}. In terms of Bayesian inversion, this process of identification of the most probable model corresponds to the conjunction of the prior and theoretical probabilities, as indicated in Figure A-1c and d of Appendix A. The size of the window used in the weighting function affects the value of $N_{cc}(\mathbf{m})$ and its identification power.

Several snapshots of the wavefield reconstructed from the seismogram depicted in Figure 4 are shown in Figure 8. The left and right panels correspond to the vertical and horizontal components, respectively. From top to bottom, the panels represent different time snapshots of the wavefield around the moment when the waves reconstructed from recorded data focus at the location of the microearthquake (8c and 8d). Similarly, several snapshots of the wavefield reconstructed from the vertical component of the seismogram depicted in Figure 4 are shown in Figure 9. The left and right panels correspond to wavefield reconstruction using the P-wave and S-wave velocities, respectively. From top to bottom, the panels rep-

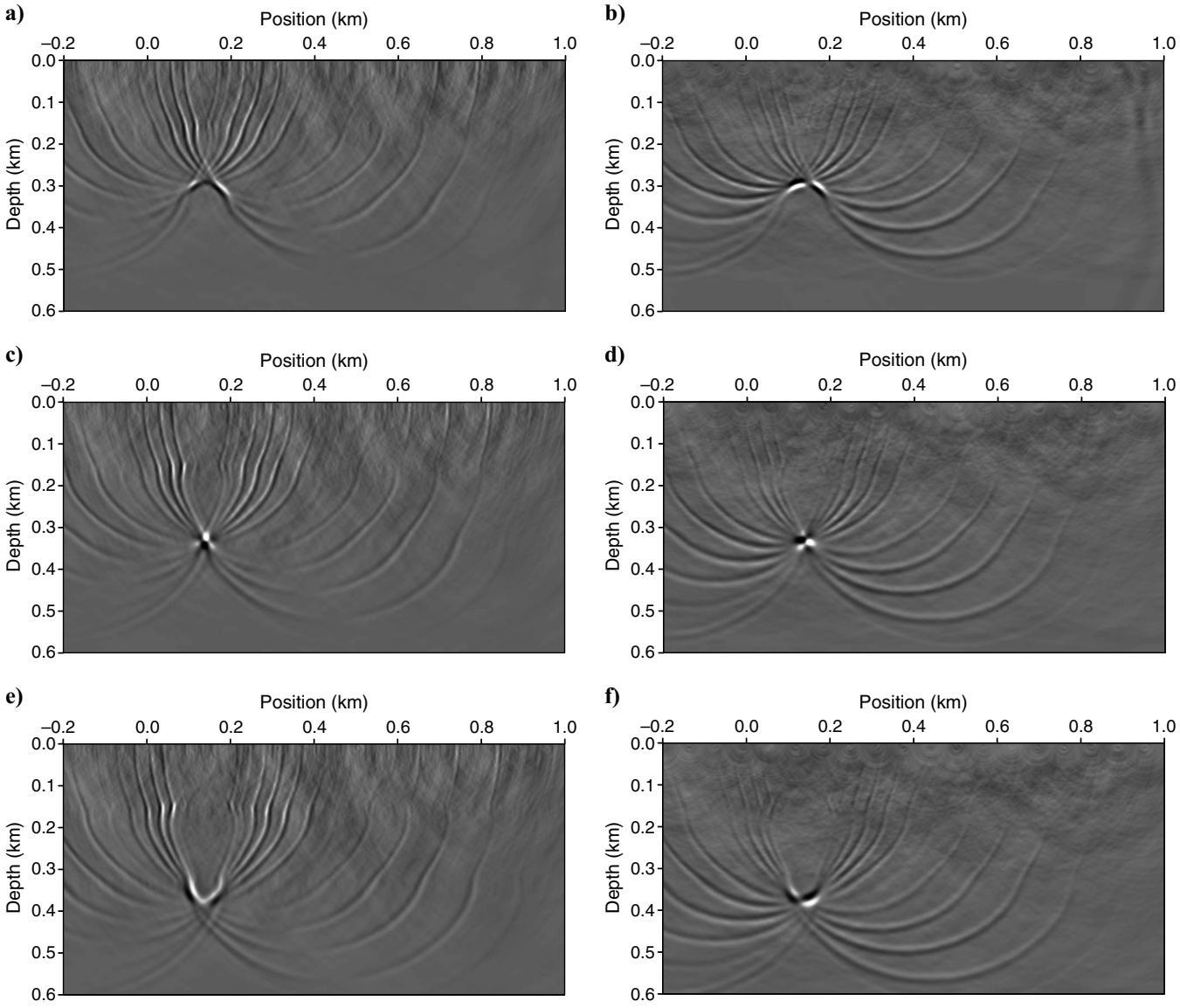


Figure 8. Snapshots of the elastic wavefield reconstructed using the elastic wave equation using the recorded multicomponent seismograms as a source. The left and right panels correspond to the vertical and horizontal components, respectively. From top to bottom, the panels represent different time snapshots of the wavefield around the moment when the waves reconstructed from recorded data focus at the location of the microearthquake (c and d).

Downloaded 16 Jul 2010 to 138.67.12.184. Redistribution subject to SEG license or copyright; see Terms of Use at http://segdl.org/

resent different time snapshots of the wavefield around the moment when the waves reconstructed from recorded data focus at the location of the microearthquake (9c and 9d).

We assume that there is no error associated with the theoretical information but that errors are introduced by the measurement uncertainty of the observed data. We also assume that the error follows a Gaussian distribution, and we give the highest probability to the model that generates the smallest data misfit. The probability density function based on the normalized crosscorrelation given by equation 6 is

$$\sigma_{\mathfrak{M}}(\mathbf{m}) = \rho_{\mathfrak{M}}(\mathbf{m}) e^{-\frac{(1-Ncc)^2}{2C_d}}, \tag{7}$$

where C_d is the measurement uncertainty. The larger the value of C_d, the flatter the distribution of $\sigma_{\mathfrak{M}}(\mathbf{m})$. When C_d is small, $\sigma_{\mathfrak{M}}(\mathbf{m})$ tends toward a delta function. To account for the unknown data-measurement uncertainty, we choose a value of C_d corresponding to 0.8 of the peak value of the Gaussian function assumed for the error distribution in the data.

We consider source identification using wavefields reconstructed from various subsets of the recorded seismograms and wave equation. Figure 10 shows the normalized crosscorrelation for vector wavefields reconstructed with the elastic wave equation. Similarly, Figure 11 shows the normalized crosscorrelation for scalar wavefields reconstructed using the acoustic wave equation from the vertical component of the recorded seismograms and the P-wave or S-wave velocities, respectively. In all cases, the left panels depict the normalized crosscorrelation function of position and time, and the right panels depict the normalized crosscorrelation at the time of maximum energy, overlain by contours indicating confidence in the

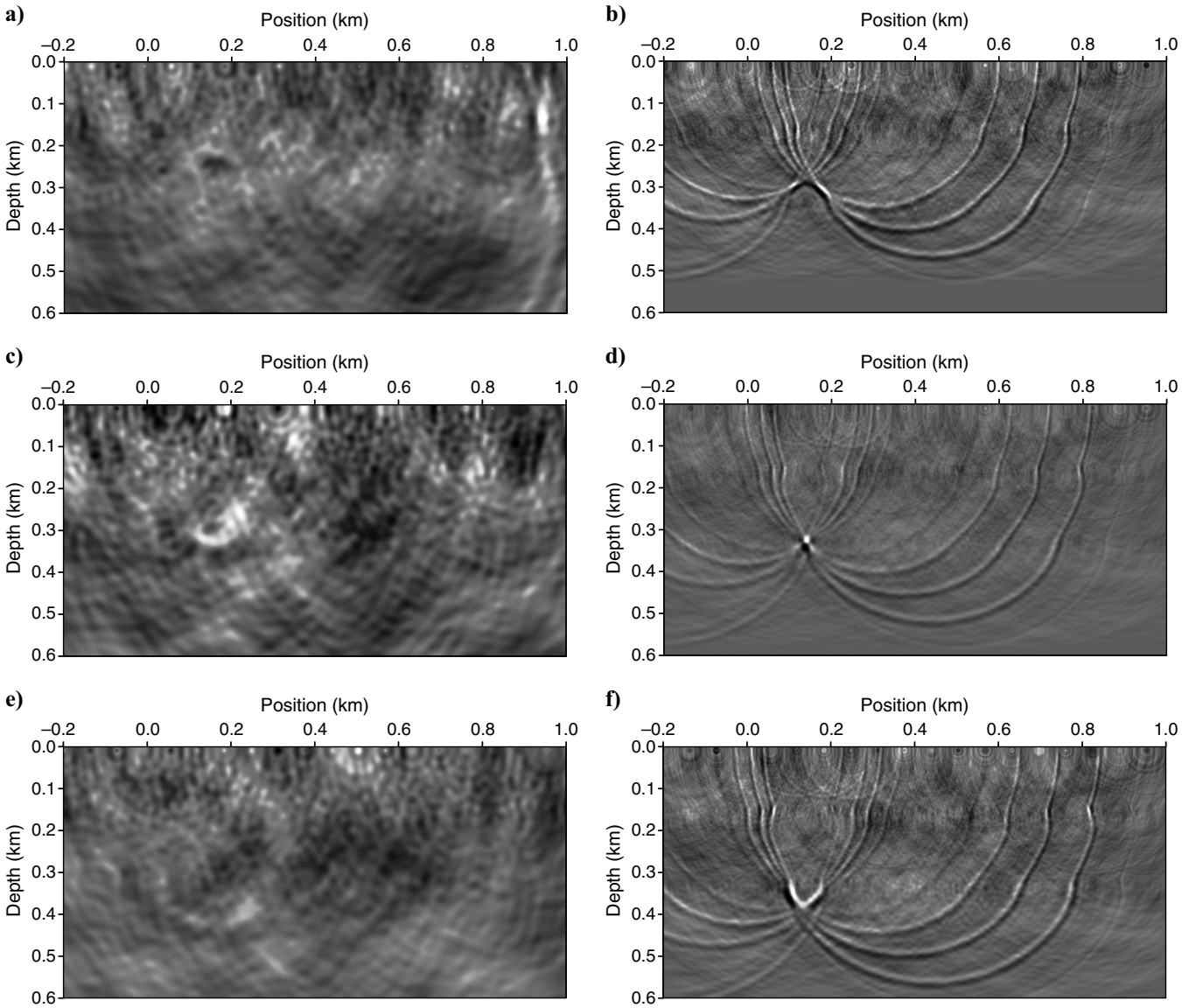


Figure 9. Snapshots of the acoustic wavefield reconstructed using the acoustic wave equation using the vertical component of the recorded seismograms as a source. The left and right panels correspond to wavefield reconstruction using the P-wave and S-wave velocities, respectively. From top to bottom, the panels represent different time snapshots of the wavefield around the moment when the waves reconstructed from recorded data focus at the location of the microearthquake (c and d).

Downloaded 16 Jul 2010 to 138.67.12.184. Redistribution subject to SEG license or copyright; see Terms of Use at http://segdl.org/

source identification. All figures represent the normalized crosscorrelation extracted at the optimal source orientation, which is 30° in this example.

In the case of imaging with the full elastic wave equation, the maximum N_{cc} value is 0.96 at $x = 0.14$ km, $z = 0.34$ km, $\tau = 0.045$ s, and $\theta = 30°$. However, the N_{cc} value is 0.95 at $\theta = 35°$. These two values are very close to each other, and it would be unwise to pick one without taking the other into consideration. Therefore, instead of selecting a single model as the answer, we construct a probability distribution characterizing various models and their likelihood to represent sources of microearthquakes.

From the analysis of these figures, we can conclude that the S-wave mode is the most energetic and that it controls the resolution of the source identification. The contours of equal confidence in Figure 11a indicate better focusing than the similar contours in Figure 11c. Furthermore, we can also conclude that we could use either the full elastic wavefields or acoustic wavefields, reconstructed from subsets of the recorded seismograms, for source identification. This fact has significant cost implications because database construction and wavefield reconstruction with the acoustic wave equation are significantly cheaper than reconstruction using the elastic wave equation.

Next we illustrate the methodology discussed in the preceding section in the case of a 3D example with a realistic acquisition geometry. The receiver layout is shown in Figure 12, and the velocity model shown in Figure 13 is a horizontal extension of the velocity used in the preceding model. The calculation is done on a grid of $x \times y \times z = 366 \times 350 \times 91$ nodes with a grid spacing of 4 m. The location of the explosive source is $x,y,z = -17$ m, -62 m, 200 m. The recorded seismogram is shown in Figure 14a. We assume that

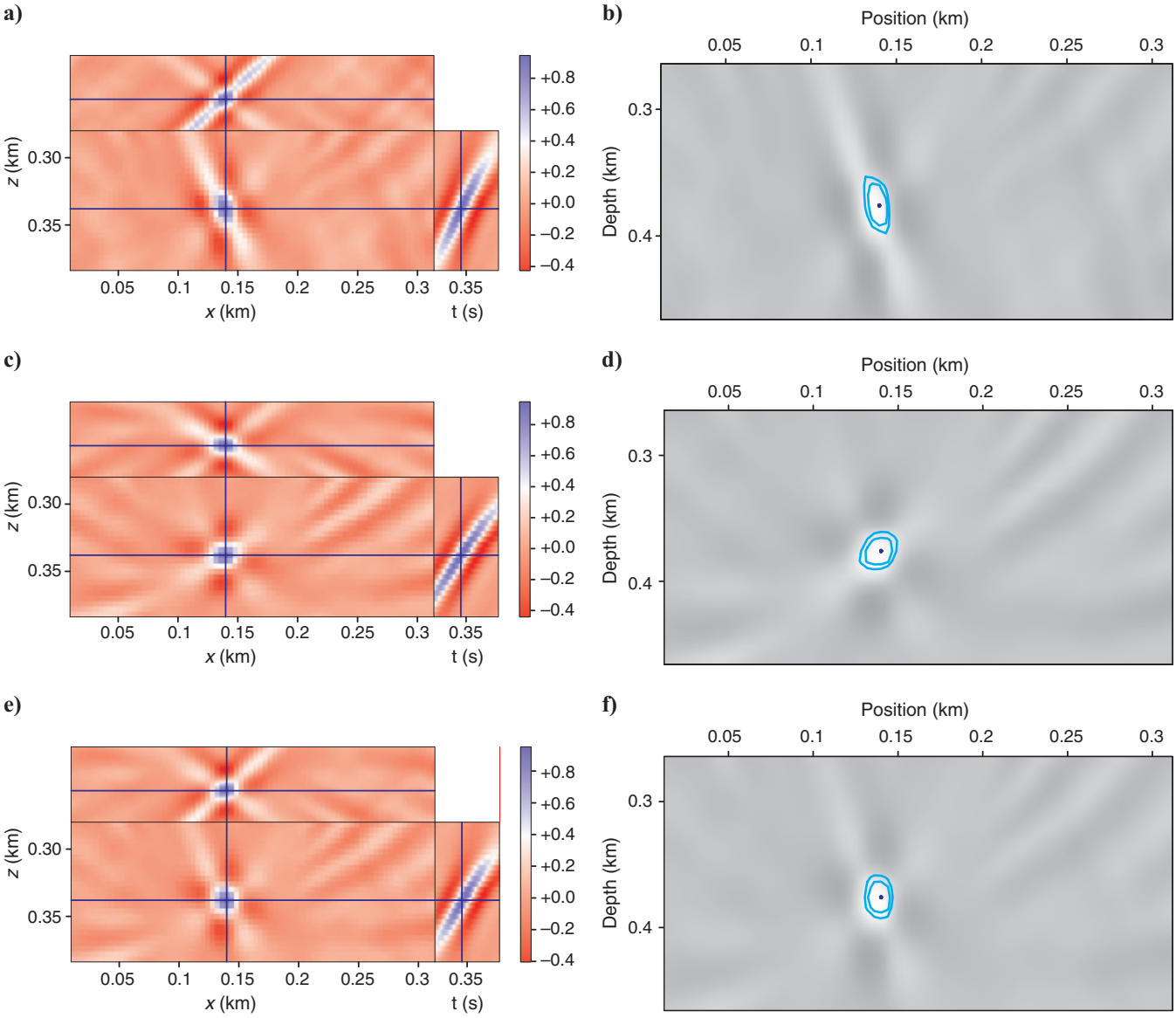


Figure 10. Representation of the (left) normalized crosscorrelation and (right) probability density functions for microearthquake identification using different types of seismic wavefields. Parts (a and b) use the vertical component of the reconstructed elastic wavefield, and (c and d) use the horizontal component of the reconstructed elastic wavefield. Panels (e and f) use the entire vector wavefield for the crosscorrelation.

Downloaded 16 Jul 2010 to 138.67.12.184. Redistribution subject to SEG license or copyright; see Terms of Use at http://segdl.org/

the data are contaminated with random noise, as illustrated in Figure 14b. The S/N for this example is approximately 0.07, which makes it impossible to pick events from the seismograms with sufficient precision for use in event identification. Because of the higher computational cost of modeling in a 3D space, we design a wavefield database on a $9 \times 9 \times 9$ grid with a spacing of 16 m in all directions. To maintain consistency with the previous section, we choose a measurement uncertainty of 0.95.

For the synthetic seismogram, one snapshot of the probability is shown in Figure 15. The intersections of the blue lines indicate that

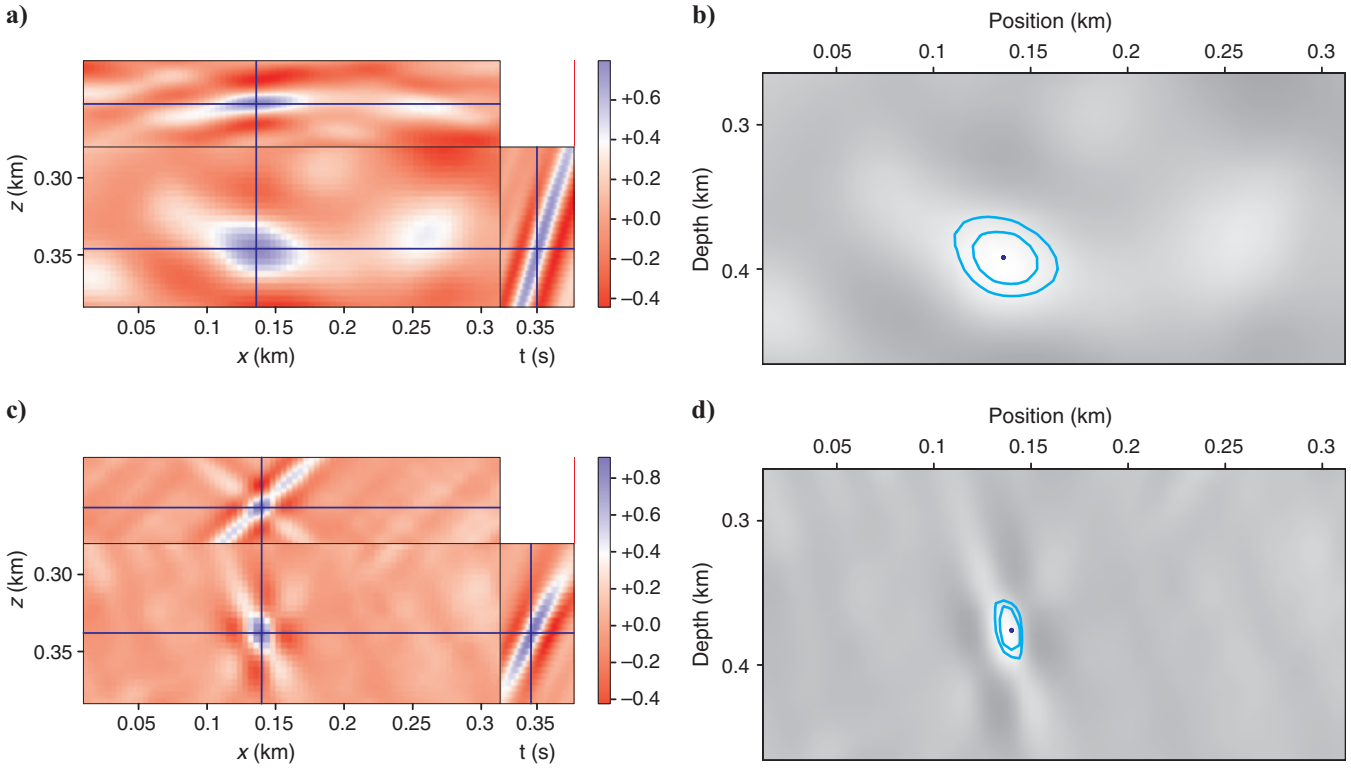


Figure 11. Representation of the (left) normalized crosscorrelation and (right) probability density functions for microearthquake identification using different types of seismic wavefields. Parts (a and b) use the wavefield reconstructed from the vertical component of the recorded seismograms using the acoustic wave equation with the P-wave velocity. Parts (c and d) use the wavefield reconstructed from the vertical component of the recorded seismograms using the acoustic wave equation with the S-wave velocity.

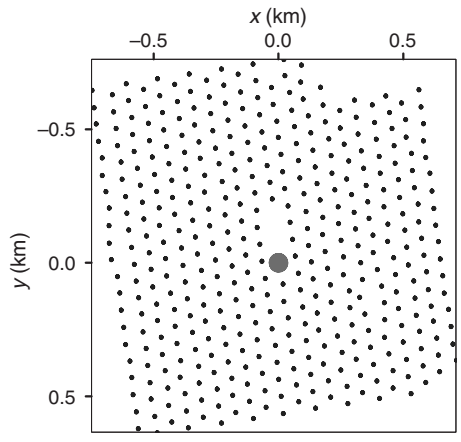


Figure 12. Geometry of a 3D surface-monitoring experiment. The large dot represents the wellhead, and the small dots represent receivers.

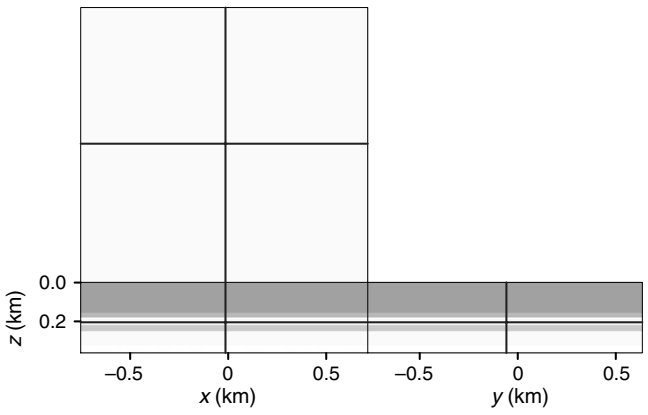


Figure 13. 3D velocity model used for the experiment described in Figure 12.

Downloaded 16 Jul 2010 to 138.67.12.184. Redistribution subject to SEG license or copyright; see Terms of Use at http://segdl.org/

the location of the maximum probability value is about 0.87. This inferred position of the source is {East, north, depth} = {−21 m, −50 m,192 m}, whereas the true source location is {−17 m, −62 m,200 m}. Several snapshots of the reconstructed wavefield are shown in Figure 16. Here, the intersections of the dark lines indicate the location with the highest probability value, as derived from Figure 15, which is also the location of maximum wavefield.

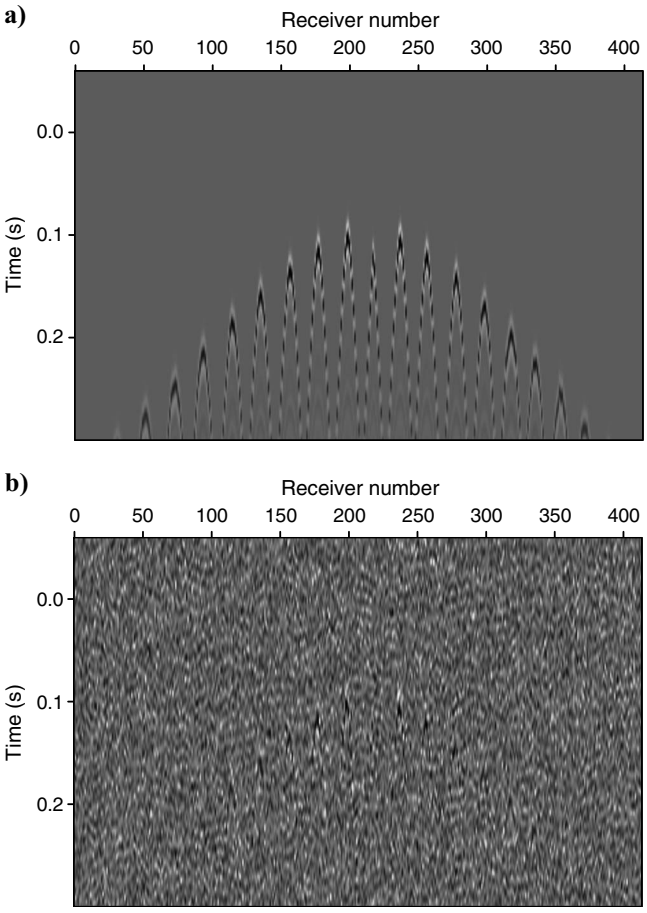


Figure 14. Synthetic seismograms of the 3D receiver geometry depicted in Figure 12. The panels correspond to the simulated data (a) with and (b) without random noise. A total of 1801 time steps with an increment of 0.2 ms is calculated. The S/N is 0.07.

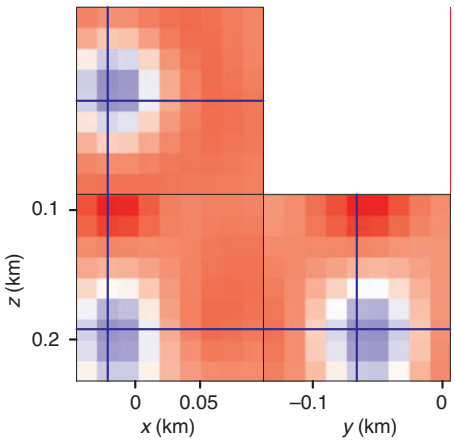


Figure 15. Probability of microearthquake occurrence function of space at the time of maximum crosscorrelation between the observed and predicted data. Grid lines indicate the correct position of the microearthquake source.

INDUCED FRACTURE EXAMPLE

In the preceding sections, we demonstrate microearthquake location in the case when only one seismic event occurs in a region during a time interval. However, a more common situation is that multiple microseismic events occur more or less at the same time and overlap in space during a given time interval. In this section, we

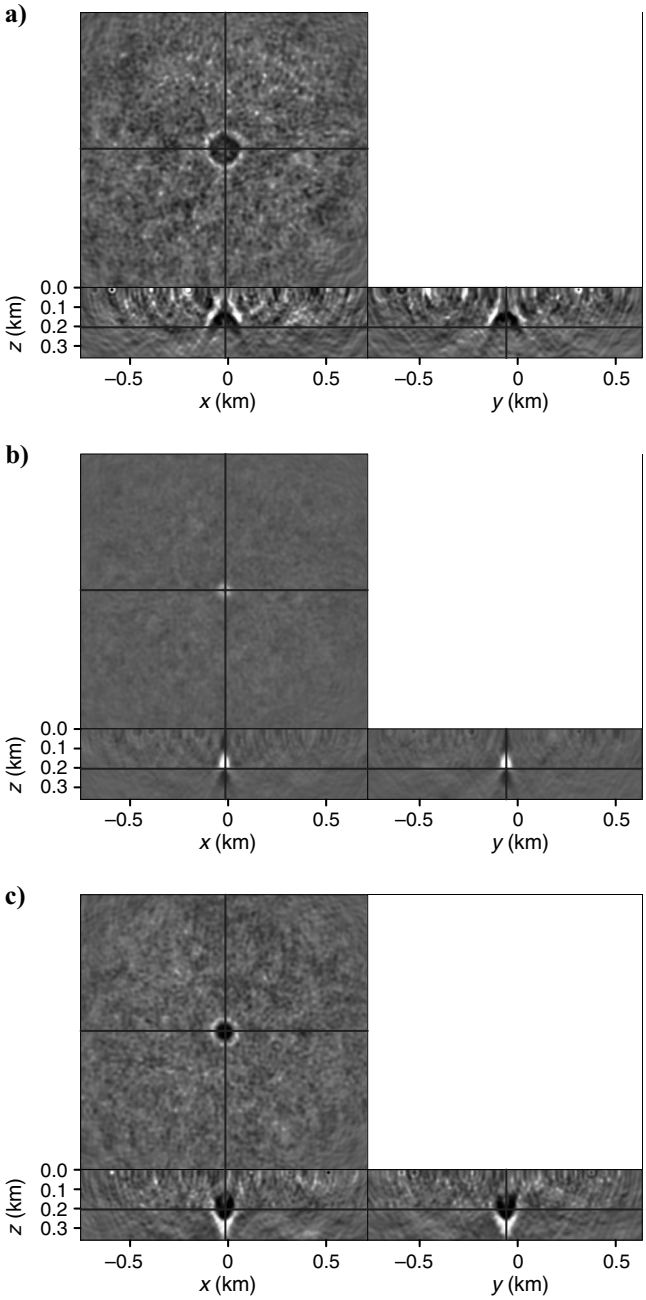


Figure 16. Snapshots of the reconstructed acoustic wavefield from the synthetic data in Figure 14b. (a, b, and c) are the snapshots before, at, and after the time of the focus of wavefield, respectively.

Downloaded 16 Jul 2010 to 138.67.12.184. Redistribution subject to SEG license or copyright; see Terms of Use at http://segdl.org/

demonstrate our methodology on another example with multiple events occurring at nearby locations and in a short period of time. The motivation for such an experiment derives from field observations about how fractures propagate during fluid injection. By spatially mapping the signals emitted by microearthquakes, we can monitor the extensions of fractures (Keppler et al., 1983; Rutledge and Phillips, 2003). Numerous field observations indicate that the seismic zone surrounds the fractures and forms an elongated pattern (House, 1987; Phillips et al., 1998; Rutledge and Phillips, 2003).

In this numerical experiment, we assume that the microseismic events are distributed along a fracture located at $z = 0.326$ km, as indicated in Figure 17. The opening of this fracture simulates high-pressure steam injected into the borehole located at $x = 0$ km. The triggering time of microseismic events varies linearly with the distance from the injection point. The difference between the origin

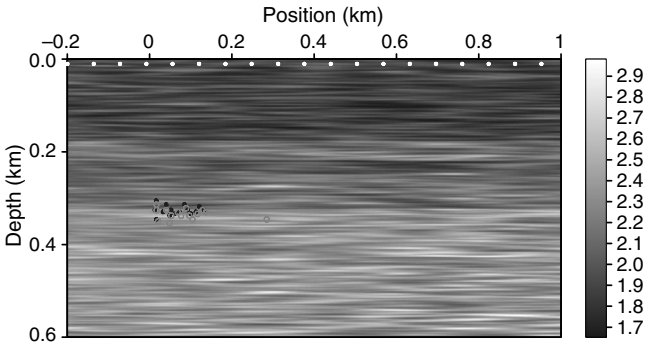


Figure 17. Synthetic model simulating an expanding fracture in a reservoir. Dots located at $z = 0$ km represent receivers, and dots located at $z = 0.3$ km represent the positions of microseismic events. Empty circles depict the inferred source positions.

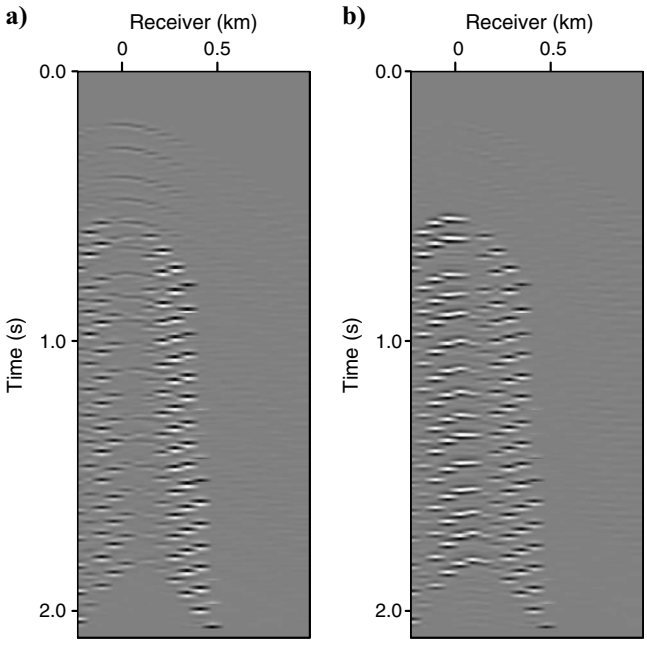


Figure 18. Synthetic seismogram corresponding to the model depicted in Figure 17. A total of 22,000 time steps with an increment of 0.1 ms is calculated. Parts (a and b) correspond to the vertical and horizontal components, respectively.

times of nearby events is greater than one period. For simplicity, we assume that the magnitude of all microearthquakes is the same and that the sources are characterized by Ricker wavelets with a dominant frequency of 30 Hz. We also assume that all microearthquakes are characterized by double-couple sources with a fixed orientation of 20°.

Figures 18 and 19 show the simulated seismograms characterizing all the events. The seismogram in Figure 19 is contaminated with two types of noise. The first type of noise is caused by model heterogeneities that we assume we do not know in the imaging process. The second type of noise is random and band limited and describes an experiment run in a noisy environment. The frequency band of the random noise is 0–140 Hz, overlapping with the microearthquake band. The S/N for this example is as low as 0.1. We assume that measurement uncertainties are 0.64, which corresponds to a radius of approximately half a wavelength for the posterior probability contour line of 0.8. This is an arbitrary choice that may change from region to region depending on the local level of uncorrelated noise. We simulate 15 microearthquakes and attempt to locate all of them with our methodology.

Figure 20 shows the normalized crosscorrelation for vector wavefields reconstructed with the elastic wave equation. In all cases, the left panels depict the normalized crosscorrelation function of position and angle of the double-couple source, and the right panels depict the normalized crosscorrelation at the time of maximum energy, overlain by contours indicating confidence in the source identification. All figures represent the normalized crosscorrelation extracted

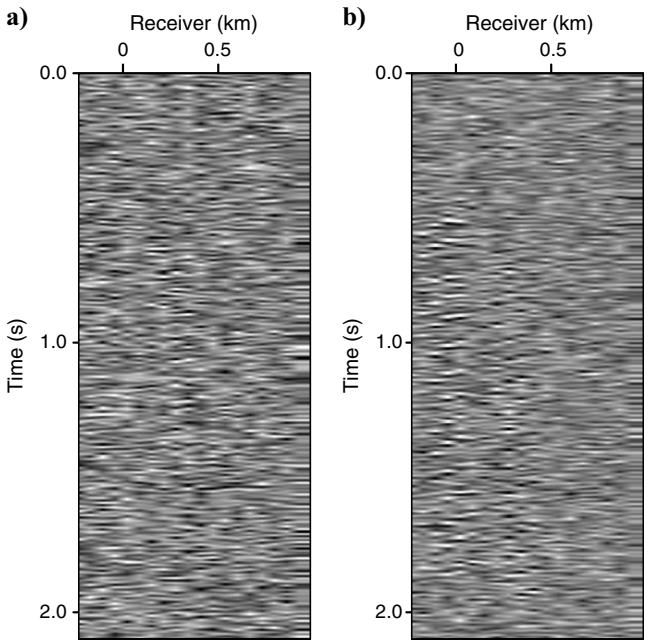


Figure 19. Synthetic seismogram corresponding to the model depicted in Figure 17. A total of 22,000 time steps with an increment of 0.1 ms is calculated. The panels correspond to the (a) vertical and (b) horizontal components. The data are corrupted with random noise, and the S/N for this experiment is 0.1. Microearthquakes are not visible on the seismograms, so they cannot be picked for use with conventional location techniques.

Downloaded 16 Jul 2010 to 138.67.12.184. Redistribution subject to SEG license or copyright; see Terms of Use at http://segdl.org/

at the inferred focus time. The contours shown indicate the probability of earthquake occurrence at various times and range from 0.8 to 0.9 with an interval of 0.1.

Table 1 summarizes the inversion results by comparing the true source parameters $\{z_t, x_t, \tau_t, \theta_t\}$ with the inferred source parameters $\{z_d, x_d, \tau_d, \theta_d\}$. Figure 17 is a graphical representation of the coordinates contained in this table. Although in this example we do not locate exactly all existing microearthquakes, we regard this experiment as a success because we obtain a good representation of the direction and speed of fracture propagation in a difficult setting characterized by low S/N and sparse data acquisition. We also see that the inferred source position is typically contained within the contour of probability equal to 0.8, which corresponds to approximately half of the signal wavelength. For example, in the case of event number 4, the true source parameters are {0.314 km, 0.040 km, 0.386 s, 20°}, whereas the inferred source parameters are {0.326 km, 0.040 km, 0.380 s, 25°}. The vertical difference is 12 m, which is approximately equal to half of the dominant S-wave wavelength. This is shown in Figure 20d by the presence of the dot indicating the true source position on the contour of 0.8 probability on the inferred position. Furthermore, the true double-couple source plane dips at 20°, whereas the inferred double-couple source plane dips at 25°.

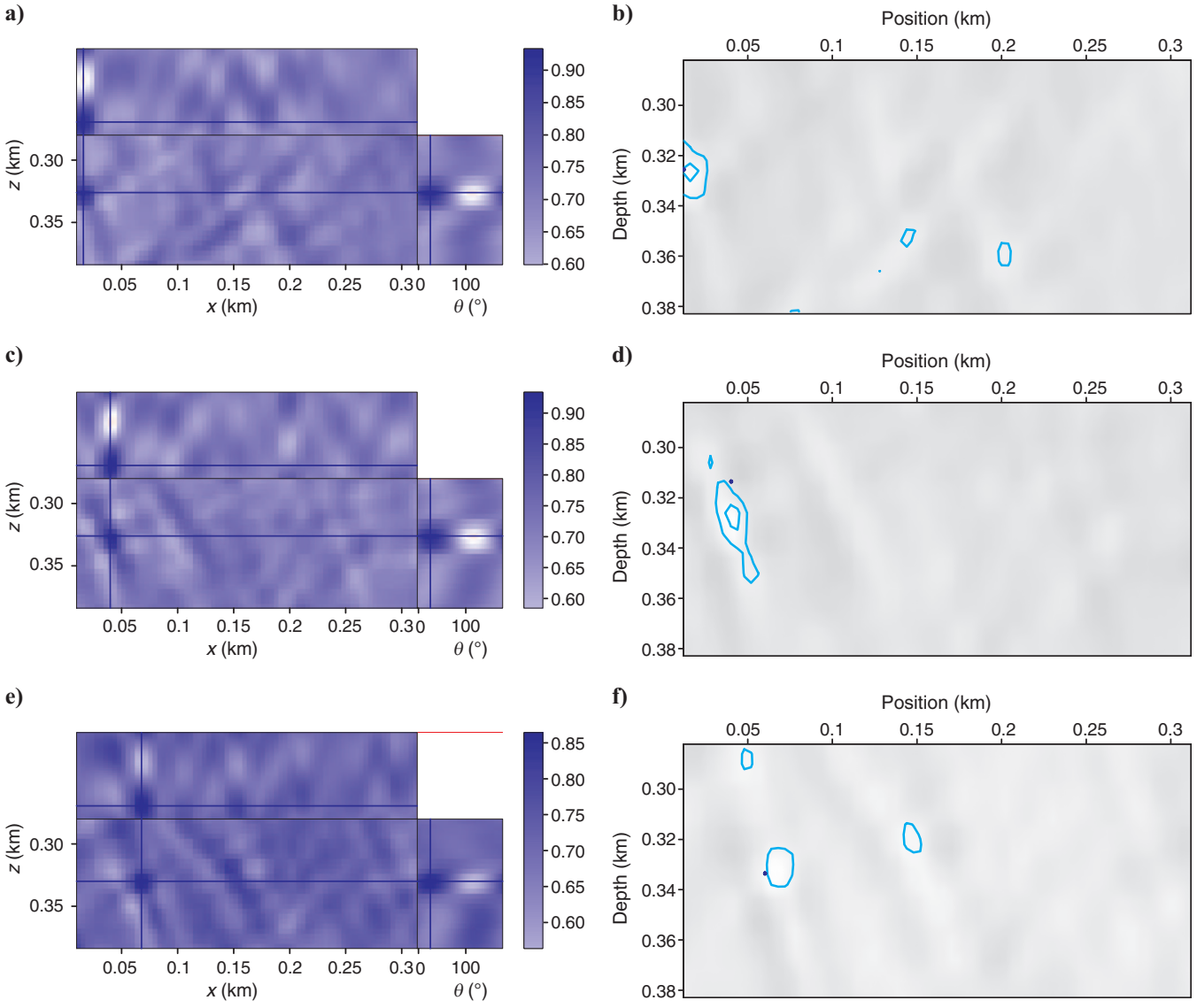


Figure 20. Snapshots of the posterior probability distribution of microseismic events. Each part corresponds to a different event located at a different time. Crosslines identify the position of the microearthquake source function of space and orientation of the double-couple source. The maximum value identifies not only the correct position of the microearthquake but also the correct orientation of the fracture plane, 20° in this case.

Downloaded 16 Jul 2010 to 138.67.12.184. Redistribution subject to SEG license or copyright; see Terms of Use at http://segdl.org/

Table 1. A comparison between the true and detected source parameters.

	z_t (km)	z_d (km)	x_t (km)	x_d (km)	τ_t (s)	τ_d (s)	θ_t (°)	θ_d (°)
0	0.326	0.326	0.012	0.016	0.020	0.025	20	25
1	0.306	0.318	0.016	0.016	0.116	0.114	20	20
2	0.346	0.350	0.016	0.020	0.206	0.209	20	25
3	0.326	0.346	0.032	0.282	0.296	0.292	20	0
4	0.314	0.326	0.040	0.040	0.386	0.380	20	25
5	0.326	0.338	0.052	0.052	0.476	0.472	20	20
6	0.338	0.354	0.048	0.048	0.566	0.557	20	30
7	0.334	0.330	0.060	0.068	0.656	0.663	20	25
8	0.330	0.338	0.072	0.076	0.746	0.744	20	20
9	0.318	0.326	0.084	0.088	0.836	0.835	20	25
10	0.326	0.338	0.092	0.096	0.926	0.921	20	25
11	0.334	0.346	0.100	0.104	1.016	1.010	20	15
12	0.330	0.334	0.112	0.116	1.106	1.107	20	25
13	0.322	0.330	0.120	0.128	1.196	1.193	20	20
14	0.326	0.330	0.132	0.140	1.286	1.284	20	25

CONCLUSION

We present a method for automatic microearthquake location using Bayesian inversion theory. Our method exploits the unique shape of wavefields partially refocused at the source position. This method does not require picking of arrival times but relies on wavefield focusing obtained by time reversal. Our method not only identifies the spatial location of the source but also specifies the origin time of the source and the orientation of the double-couple sources characterizing fault planes. Furthermore, because we are using a probabilistic approach to microearthquake location, our method provides confidence maps of microearthquake locations that can be used for risk assessment. Synthetic data examples demonstrate the robustness of the method and its applicability to situations when microearthquakes occur in close succession in a small region in space and are recorded in a noisy environment with a S/N as low as 0.1.

ACKNOWLEDGMENTS

This work was supported by ExxonMobil URC. We are grateful to Mike Payne, Jie Zhang, Rongrong Lu, Alex Martinez, and Anupama Venkataraman at ExxonMobil URC for access to data, technical discussions, and financial support of this project.

APPENDIX A

BAYESIAN INVERSION THEORY

This appendix summarizes the main elements of Bayesian inversion theory, which characterizes our state of knowledge in a probabilistic manner through the use of probability density functions (PDFs) linking model and data parameters (Jaynes, 2003). We can define two states of knowledge. The prior state characterizes our knowledge about the model and data parameters before any measurements are taken. This information is based on our general knowledge of the phenomenon under investigation and on the distribution of model parameters and assumptions about the reliability of our measurements. The posterior state characterizes our knowledge about the model and data parameters after measurements are made and data are processed and interpreted. Both states of knowledge are characterized by PDFs that link model and data parameters. Ideally, the measurements help refine the prior state into the posterior state of knowledge, which provides a tighter connection between model and data parameters.

In describing Bayesian inversion theory, we need to discuss the following elements: model ($\mathbf{m}$) and model space, data ($\mathbf{d}$) and data space, the prior state of knowledge (a priori PDF $\rho(\mathbf{m},\mathbf{d})$), the theoretical relations between model and data (theoretical PDF $\Theta(\mathbf{m},\mathbf{d})$), and the posterior state of knowledge (a posteriori PDF $\sigma(\mathbf{m},\mathbf{d})$).

Model and data spaces

The model space ($\mathfrak{M}$) is composed of a set of individual models which can be denoted by i ($i \in \{1,2,\ldots,N\}$). The model space represents all the models that can possibly characterize the physical phenomenon under investigation.

The data space $\mathfrak{D}$ is composed of all instrumental responses to the investigated models which can be denoted by $\mathbf{d}_i$ ($i \in \{1,2,\ldots,M\}$). The data space represents all data that can possibly be recorded and that characterize the physical phenomenon under investigation.

A priori probability density $\rho(\mathbf{m},\mathbf{d})$

We describe $\rho(\mathbf{m},\mathbf{d})$ by a joint PDF over the model and data spaces. This prior information is independent of any measurement. Furthermore, in the special case when the prior information on the model space $\rho_{\mathfrak{M}}(\mathbf{m})$ is independent of the prior information on the data space $\rho_{\mathfrak{D}}(\mathbf{d})$, the a priori probability density function $\rho(\mathbf{m},\mathbf{d})$ is (Tarantola, 2005)

$$\rho(\mathbf{m},\mathbf{d}) = \rho_{\mathfrak{D}}(\mathbf{d})\rho_{\mathfrak{M}}(\mathbf{m}), \qquad \text{(A-1)}$$

where $\rho_{\mathfrak{D}}(\mathbf{d})$ describes the measurement uncertainty of the observed data and $\rho_{\mathfrak{M}}(\mathbf{m})$ illustrates our confidence in the chosen model parameters.

Downloaded 16 Jul 2010 to 138.67.12.184. Redistribution subject to SEG license or copyright; see Terms of Use at http://segdl.org/

Two examples of a priori probability density functions are shown in Figures A-1a and A-2a. The vertical axis represents the value of the probability that a particular model characterizes the physical system under investigation. In Figure A-1a, $\rho(\mathbf{m},\mathbf{d}) = \rho_{\mathfrak{M}}(\mathbf{m})\delta(\mathbf{d} - \mathbf{d}^{\text{obs}})$, where $\mathbf{d}^{\text{obs}}$ denote the observed data, and the a priori probability in the model space is a step function. In this case, no error is associated with the observed data. In Figure A-2a, $\rho(\mathbf{m},\mathbf{d}) = \rho_{\mathfrak{M}}(\mathbf{m})e^{-(\mathbf{d}-\mathbf{d}^{\text{obs}})^2/2C_d}$, where $\rho_{\mathfrak{M}}(\mathbf{m})$ is a tapered step function and C_d is the measurement uncertainty of the data. We assume that the data are distributed according to a Gaussian distribution.

Homogeneous probability density $\mu(\mathbf{m},\mathbf{d})$

To remove the effect of the discretization of the model and data parameters, we define a homogeneous PDF $\mu(\mathbf{m},\mathbf{d})$ whose role is to balance the discrete model and data spaces. By definition, the homogeneous probability distribution states that a probability assigned to each region of the space is proportional to the volume of the region (Mosegaard and Tarantola, 2002). In the special case when the homogeneous probability densities on the model and data spaces are independent, $\mu(\mathbf{m},\mathbf{d})$ is expressed as

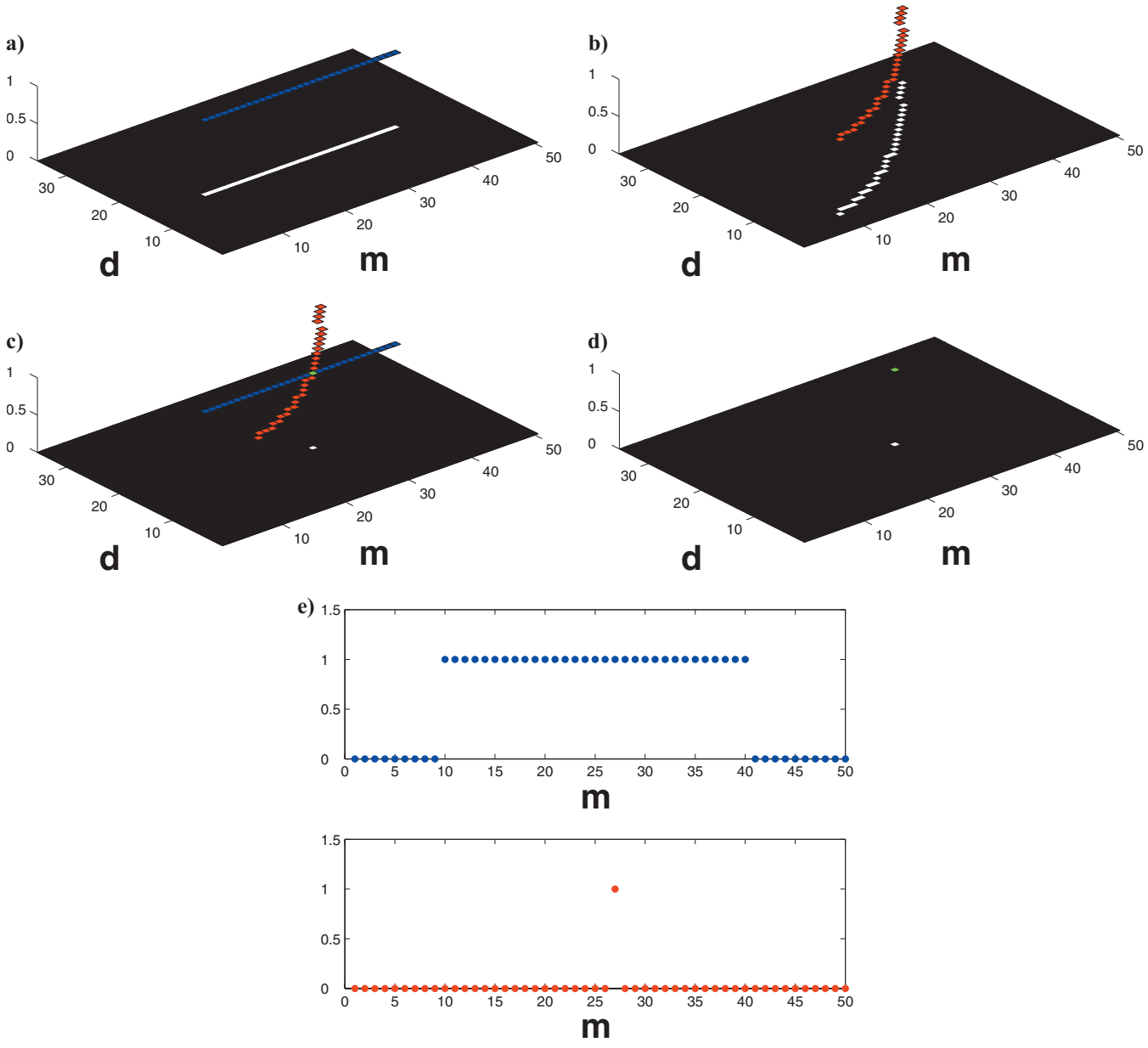


Figure A-1. (a) A priori probability density function $\rho(\mathbf{m},\mathbf{d})$ represented by a delta function corresponding to $\rho_{\mathfrak{M}}(\mathbf{m})$ which is also represented by a step function. (b) Theoretical probability density function $\Theta(\mathbf{m},\mathbf{d})$ representing the physical relationship given by $G(\mathbf{m})$ and assumed to be exact. (c) Conjunction between $\rho(\mathbf{m},\mathbf{d})$ and $\Theta(\mathbf{m},\mathbf{d})$. (d) A posteriori probability density function $\sigma(\mathbf{m},\mathbf{d})$ indicating that the solution to the Bayesian inversion problem is given by a single model. (e) Comparison between the marginal probabilities showing $\rho_{\mathfrak{M}}(\mathbf{m})$ in the upper panel and $\sigma_{\mathfrak{M}}(\mathbf{m})$ in the lower panel.

Downloaded 16 Jul 2010 to 138.67.12.184. Redistribution subject to SEG license or copyright; see Terms of Use at http://segdl.org/

$$\mu(\mathbf{m},\mathbf{d}) = \mu_{\mathfrak{D}}(\mathbf{d})\mu_{\mathfrak{M}}(\mathbf{m}), \qquad \text{(A-2)}$$

where $\mu_{\mathfrak{M}}(\mathbf{m})$ is the homogeneous probability density on the model space and $\mu_{\mathfrak{D}}(\mathbf{d})$ is the homogeneous probability density on the data space.

For example, in spherical coordinates, the volume of a standard region is $dV(r,\theta,\varphi) = r^2 \sin\theta dr d\theta d\varphi$. The homogeneous probability distribution is $\mu = kr^2 \sin\theta$, where k is an arbitrary constant. For 3D Cartesian coordinates, $dV(x,y,z) = dxdydz$ and μ is a constant.

Theoretical probability density $\Theta(\mathbf{m},\mathbf{d})$

The theoretical probability density $\Theta(\mathbf{m},\mathbf{d})$ describes the correlations between the model and data parameters. The defined relationship corresponds to a physical law and may incorporate uncertainties associated with theory, for example, due to assumptions or simplifications of the physical law or due to imperfect knowledge of the physical parameters underlying it. The theoretical probability density $\Theta(\mathbf{m},\mathbf{d})$ can be expressed as

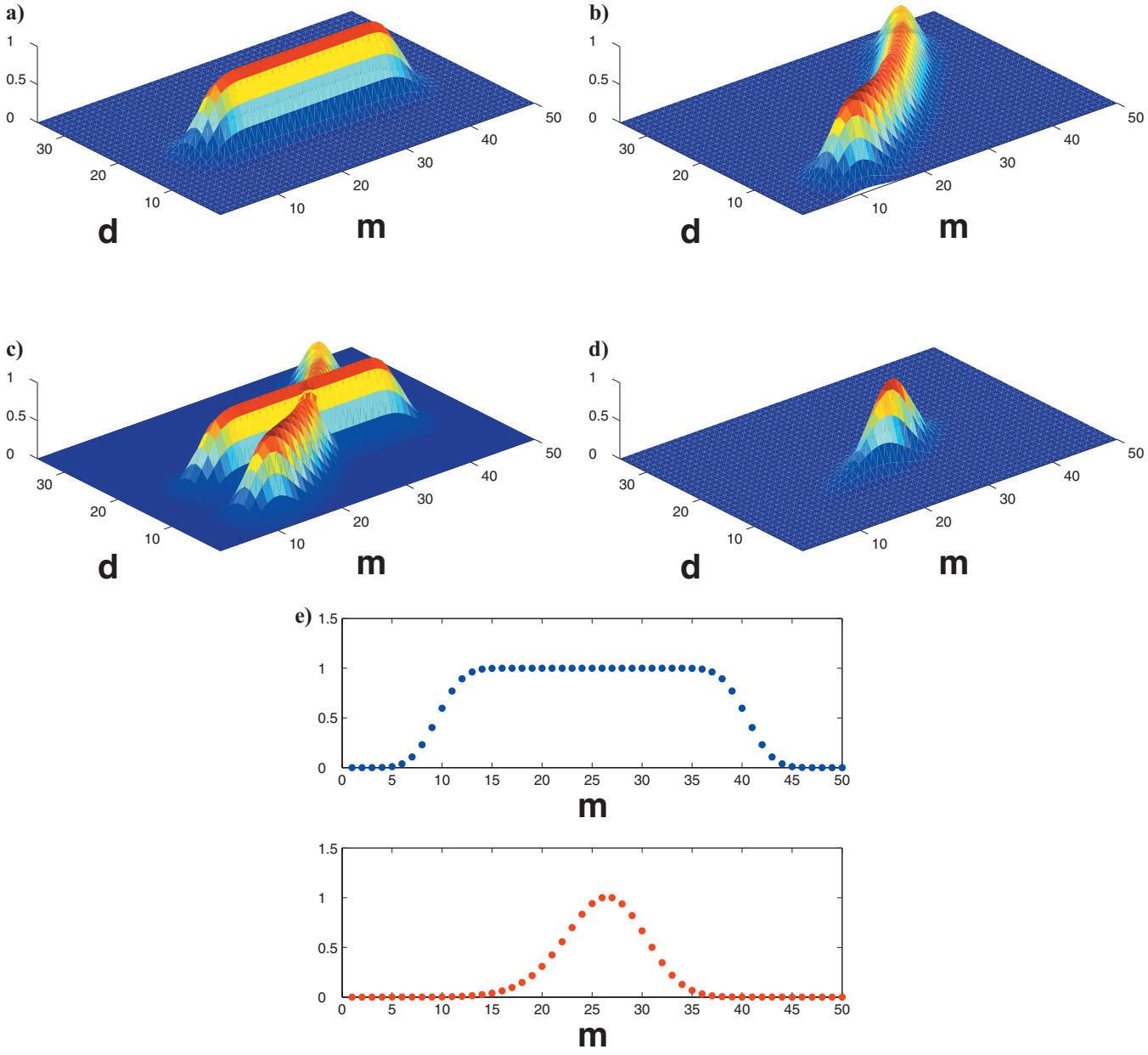


Figure A-2. (a) A priori probability density function $\rho(\mathbf{m},\mathbf{d})$ represented by a Gaussian function corresponding to $\rho_{\mathfrak{M}}(\mathbf{m})$ represented by a tapered step function. (b) Theoretical probability density function $\Theta(\mathbf{m},\mathbf{d})$ representing the physical relationship given by $G(\mathbf{m})$ and assumed to be uncertain. (c) Conjunction between $\rho(\mathbf{m},\mathbf{d})$ and $\Theta(\mathbf{m},\mathbf{d})$. (d) A posteriori probability density function $\sigma(\mathbf{m},\mathbf{d})$ indicating that the solution to the Bayesian inversion problem is given by several models corresponding to the uncertainties of the prior and theoretical probability density functions. (e) Comparison between the marginal probabilities showing $\rho_{\mathfrak{M}}(\mathbf{m})$ in the upper panel and $\sigma_{\mathfrak{M}}(\mathbf{m})$ in the lower panel.

Downloaded 16 Jul 2010 to 138.67.12.184. Redistribution subject to SEG license or copyright; see Terms of Use at http://segdl.org/

$$\Theta(\mathbf{m},\mathbf{d}) = \theta(\mathbf{d}|\mathbf{m})\mu_{\mathfrak{M}}(\mathbf{m}), \tag{A-3}$$

where $\theta(\mathbf{d}|\mathbf{m})$ describes the probability distribution of data for the given kernel function and model, and $\mu_{\mathfrak{M}}(\mathbf{m})$ is the marginal probability defined in the preceding section. In Figure A-1b, $\theta(\mathbf{d}|\mathbf{m}) = \delta(\mathbf{d} - G(\mathbf{m}))$, where $G(\mathbf{m})$ is the kernel function that describes the physical relationship between $\mathbf{d}$ and $\mathbf{m}$. No error is associated with this kernel function. In Figure A-1b, $\theta(\mathbf{d}|\mathbf{m}) = e^{-(\mathbf{d}-G(\mathbf{m}))^2/2C_t}$, where C_t describes the theory uncertainty. The error associated with this kernel function follows a Gaussian distribution.

A posteriori probability density $\sigma(\mathbf{m},\mathbf{d})$

The conjunction between the a priori state of information $\rho(\mathbf{m},\mathbf{d})$ and the theoretical probability density function $\Theta(\mathbf{m},\mathbf{d})$, which describes the theoretical relationship between model and data, provides the a posteriori state of information $\sigma(\mathbf{m},\mathbf{d})$:

$$\sigma(\mathbf{m},\mathbf{d}) = k\frac{\rho(\mathbf{m},\mathbf{d})\Theta(\mathbf{m},\mathbf{d})}{\mu(\mathbf{m},\mathbf{d})}, \tag{A-4}$$

where k is a normalization constant that serves the purpose of keeping the area under the graph of $\sigma(\mathbf{m},\mathbf{d})$ constant. The expression for k is

$$k = \frac{1}{\int_{\mathfrak{X}} d\mathfrak{X}\rho(\mathbf{m},\mathbf{d})\Theta(\mathbf{m},\mathbf{d})/\mu(\mathbf{m},\mathbf{d})}, \tag{A-5}$$

where $\mathfrak{X} = (\mathfrak{D},\mathfrak{M})$ is the joint space of the data and the model.

The posterior information $\sigma(\mathbf{m},\mathbf{d})$ is computed based on observations. In the special case when both the model space and the data space are described in Cartesian coordinates, the posterior information is proportional to the conjunction between the prior information and the theoretical information:

$$\sigma(\mathbf{m},\mathbf{d}) \propto \rho(\mathbf{m},\mathbf{d})\Theta(\mathbf{m},\mathbf{d}). \tag{A-6}$$

Figures A-1c and A-2c show the conjunction between the $\rho(\mathbf{m},\mathbf{d})$ and $\Theta(\mathbf{m},\mathbf{d})$. In Figure A-1c, $\sigma(\mathbf{m},\mathbf{d}) \propto \delta(\mathbf{d}^{\text{obs}} - G(\mathbf{m}))$, which is shown in Figure A-1d. Figure A-2c gives the conjunction between the PDFs shown in Figure A-2a and b. Its physical meaning is that the observed data are exactly the same as the data calculated from the kernel function. In Figure A-2c, $\sigma(\mathbf{m},\mathbf{d}) \propto e^{-(\mathbf{d}^{\text{obs}}-G(\mathbf{m}))^2/2C}$, where $C = C_d + C_t$. Figure A-2d shows $\sigma(\mathbf{m},\mathbf{d})$. The probability distribution in Figure A-2d shows how well the data calculated from the kernel function explain the observed data.

The marginal probability density $\sigma_{\mathfrak{M}}(\mathbf{m})$

To provide a solution to the inversion problem, we have to transfer the information provided by $\sigma(\mathbf{m},\mathbf{d})$ to the model space. We obtain the marginal probability density in the model space $\sigma_{\mathfrak{M}}(\mathbf{m})$ by projecting $\sigma(\mathbf{m},\mathbf{d})$ onto the model space:

$$\sigma_{\mathfrak{M}}(\mathbf{m}) = \int_{\mathfrak{D}} \sigma(\mathbf{m},\mathbf{d})d\mathbf{d}. \tag{A-7}$$

The probability density function provided by $\sigma_{\mathfrak{M}}(\mathbf{m})$ indicates which models satisfy our prior knowledge on the distribution of model parameters, the theoretical relationships between model and data, and the measurement uncertainties. A comparison between $\mathfrak{M}(\mathbf{m})$ and $\sigma_{\mathfrak{M}}(\mathbf{m})$ is shown in Figures A-1e and A-2e. The distribution on $\sigma_{\mathfrak{M}}(\mathbf{m})$ is narrower on the posterior relative to the prior, indicating the tighter connection introduced by the recorded data.

Negligible theoretical uncertainties

When we assume that no uncertainty is associated with the kernel function $G(\mathbf{m})$, which describes the physical relationship between the data and the model, the theoretical probability density $\Theta(\mathbf{m},\mathbf{d})$ can be expressed as

$$\Theta(\mathbf{m},\mathbf{d}) = \delta(\mathbf{d} - G(\mathbf{m}))\mu_{\mathfrak{M}}(\mathbf{m}), \tag{A-8}$$

where $\mu_{\mathfrak{M}}(\mathbf{m})$ is a constant for models parameterized in Cartesian coordinates. The theoretical probability density $\Theta(\mathbf{m},\mathbf{d}) = 1$ equals one when the data equal the value calculated from the kernel function and zero otherwise.

In this case, the marginal probability in the model space in equation A-7 can be expressed as

$$\sigma_{\mathfrak{M}}(\mathbf{m}) = \int_{\mathfrak{D}} \sigma(\mathbf{m},\mathbf{d})d\mathbf{d} = k\int_{\mathfrak{D}} \frac{\rho(\mathbf{m},\mathbf{d})\Theta(\mathbf{m},\mathbf{d})}{\mu(\mathbf{m},\mathbf{d})}d\mathbf{d}, \tag{A-9}$$

and when $\Theta(\mathbf{m},\mathbf{d})$ is given in equation A-8, with $\rho(\mathbf{m},\mathbf{d}) = \rho_{\mathfrak{D}}(\mathbf{d})\rho_{\mathfrak{M}}(\mathbf{m})$ and $\mu(\mathbf{m},\mathbf{d}) = \mu_{\mathfrak{D}}(\mathbf{d})\mu_{\mathfrak{M}}(\mathbf{m})$, we can write,

$$\sigma_{\mathfrak{M}}(\mathbf{m}) = k\rho_{\mathfrak{M}}(\mathbf{m})\int_{\mathfrak{D}} \frac{\rho_{\mathfrak{D}}(\mathbf{d})\delta(\mathbf{d} - G(\mathbf{m}))}{\mu_{\mathfrak{D}}(\mathbf{d})}d\mathbf{d}, \tag{A-10}$$

where $\rho_{\mathfrak{D}}(\mathbf{d})$ is a function of $\mathbf{d}$ and the observed data, and $\mu_{\mathfrak{D}}(\mathbf{d})$ is a constant for data discretized in Cartesian coordinates. Thus, equation A-7 for an ideal kernel function can be written as

$$\sigma_{\mathfrak{M}}(\mathbf{m}) = \nu\rho_{\mathfrak{M}}(\mathbf{m})\rho_{\mathfrak{D}}(G(\mathbf{m}),\mathbf{d}^{\text{obs}}), \tag{A-11}$$

where

$$\nu = \int_{\mathfrak{M}} \rho_{\mathfrak{M}}(\mathbf{m})\rho_{\mathfrak{D}}(\mathbf{d},\mathbf{d}^{\text{obs}})d\mathbf{m} \tag{A-12}$$

is a constant. In equation A-11, $\sigma_{\mathfrak{M}}(\mathbf{m})$ is proportional to the product of the prior probabilities on the model and data spaces.

REFERENCES

Duncan, P. M., 2005, Is there a future for passive seismic?: First Break, **23**, 111–115.

Gajewski, D., D. Anikiev, B. Kashtan, E. Tessmer, and C. Vanelle, 2007, Localization of seismic events by diffraction stacking: 77th Annual International Meeting, SEG, Expanded Abstracts, 1287–1291.

Gajewski, D., and E. Tessmer, 2005, Reverse modelling for seismic event characterization: Geophysical Journal International, **163**, 276–284.

House, L., 1987, Locating microearthquakes induced by hydraulic fracturing in crystalline rock: Geophysical Research Letters, **14**, 919–921.

Jaynes, E. T., 2003, Probability theory: The logic of science: Cambridge University Press.

Keppler, H., C. Pearson, R. Potter, and J. Albright, 1983, Microearthquakes induced during hydraulic fracturing at the Fenton Hill HDR site: The 1982 experiments: Annual Meeting, Geothermal Resources Council, 1–9.

Lay, T., and T. C. Wallace, 1995, Modern global seismology: Academic Press.

Maxwell, S. C., and T. I. Urbancic, 2001, The role of passive microseismic monitoring in the instrumented oil field: The Leading Edge, **20**, 636–639.

Mosegaard, K., and A. Tarantola, 2002, Probabilistic approach to inverse problems, *in* W. H. K. Lee, H. Kanamori, P. C. Jennings, and C. Kisslinger, eds., International handbook of earthquake & engineering seismology—Part A: Academic Press, 237–265.

Downloaded 16 Jul 2010 to 138.67.12.184. Redistribution subject to SEG license or copyright; see Terms of Use at http://segdl.org/

Pearson, C., 1981, The relationship between microseismicity and high pore pressures during hydraulic stimulation experiments in low permeability granitic rocks: Journal of Geophysical Research, **86**, 7855–7864.
Phillips, W. S., T. D. Fairbanks, J. T. Rutledge, and D. W. Anderson, 1998, Induced microearthquake patterns and oil-producing fracture systems in the Austin chalk: Tectonophysics, **289**, 153–169.
Pujol, J., 2004, Earthquake location tutorial: Graphical approach and approximate epicentral location techniques: Seismological Research Letters, **75**, 63–74.
Rentsch, S., S. Buske, S. Lüth, and S. A. Shapiro, 2004, Location of seismicity using Gaussian beam type migration: 74th Annual International Meeting, SEG, Expanded Abstracts, 354–357.
Rutledge, J. T., and W. S. Phillips, 2003, Hydraulic stimulation of natural fractures as revealed by induced microearthquakes, Carthage Cotton Valley gas field, east Texas: Geophysics, **68**, 441–452.
Tarantola, A., 2005, Inverse problem theory and methods for model parameter estimation: Society for Industrial and Applied Mathematics.
Thurber, C. H., and N. Rabinowitz, eds., 2000, Advances in seismic event location — Modern approaches in geophysics: Kluwer Academic Publishers.
Zitová, B., and J. Flusser, 2003, Image registration methods: A survey: Image and Vision Computing, **21**, 977–1000.

Downloaded 16 Jul 2010 to 138.67.12.184. Redistribution subject to SEG license or copyright; see Terms of Use at http://segdl.org/